KRONOS FUSION ENERGY

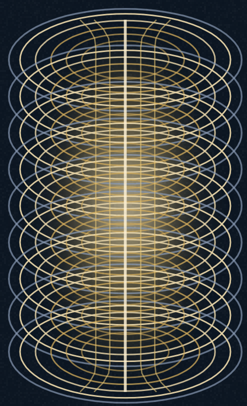

PAPER 1.3 · THE KRONOS 2026 SERIES

The REBCO High-Field Superconductor Basis: Conductor, Winding, and the Field Envelope for the Breeder Centrepost and Burner Plug

The enabling technology of compact fusion is the high-field rare-earth barium copper oxide (REBCO) magnet, and the binding engineering limit of such a magnet is not the coated...

Read it live — 3-D model · physics validator · film series

BY P I FORD, R J WEGGEL AND C WEGGEL

2026 · EDITORIAL EDITION

THE OFFICIAL RECORD

What this document is, and how to read its numbers

This is a combined editorial. It gathers, in one volume, the two design studies Kronos Fusion Energy released in 2026 — a compact spherical-tokamak tritium/helium-3 breeder and a deuterium–helium-3 tandem-mirror generator — together with the intellectual-property estate, the people, and, in the internal edition, the full commercial case. The scientific text is the same text that appears in the arXiv preprints and the journal submissions; the editorial adds the apparatus a reader needs to hold the whole program at once, and nothing in the physics is altered to fit it.

THE HONESTY STANCE IS THE ASSET

Every headline quantity carries an **evidence class** — DERIVED RECOMPUTED MEASURED REQUIREMENT — and, where a number is a modelled extrapolation rather than a demonstrated value, it is labelled as such and its downside is shown next to it. Several quantities in the underlying corpus moved after first publication; where a value has been withdrawn or restated, the record says so plainly. This is deliberate: a diligence team will find the load-bearing assumptions, so the document surfaces them first.

TWO EDITIONS

This volume is issued in two editions. The **public edition** (light) carries the physics and the design only — no dollar, price, or per-kilogram figure appears anywhere in it. The **internal edition** (dark) adds the economics, the funding architecture, and the defense-commercial analysis, and is marked *Confidential* accordingly; it is not for public distribution. Where the commercial case rests on a modelled assumption rather than a demonstrated one, it is labelled as such and its downside is shown alongside it, on the same terms as the physics.

TITLE	The Kronos Fleet — Hyperion · Aegis · MetroVolt: A Combined Design & Commercialization Study
AUTHOR	Priyanca Ford, Founder & CEO, on behalf of Kronos Fusion Energy
EDITION	2026 Combined Editorial · first issue
COMPANION WORKS	The five-paper arXiv drop — (1) Breeder, (2) Burner, (3) REBCO magnet & tape, (4) Direct Energy Conversion, (5) AI/ML/Quantum control — with matching numbered Zenodo deposits, plus the IOP journal and IAEA-FEC submissions. Patents were filed before the drop.
NAMING	Hyperion = the breeder; Aegis (defense) and MetroVolt (data-center) = one generator in two housings. Internal mode letters (D1, L) do not appear on public surfaces.
STATUS	Conceptual design & simulation study. Nothing herein is a construction commitment.

HOW TO READ THIS VOLUME

The fleet at a glance, and the way its numbers are marked

This volume opens with *Orientation*, presents the five research papers as a bound sequence, and closes with the *Apparatus*. *Foundations* sets out the three general results both machines rest on. *Paper One* is the Hyperion breeder; *Paper Two* the Aegis / MetroVolt generator; *Papers Three, Four and Five* are the enabling science — high-field REBCO magnets and tape, direct energy conversion, and the AI / ML / quantum control stack. A *Digital Twin & 3-D Model* part follows, then the *Environmental* profile. The *Economics* and levelized cost and the *Business Case* and diligence record appear in the internal edition only; the *Simulations* proof record and the Apparatus — patent portfolio, team, limitations, and sources — close both editions.

THE FLEET AT A GLANCE

	HYPERION	AEGIS	METROVOLT
Role	Strategic-isotope foundry	Defense installation power	Campus power
Machine	**Spherical tokamak**	**Tandem mirror**	**Tandem mirror**
Fuel	Deuterium–tritium	Deuterium–helium-3	Deuterium–helium-3
Delivers	Tritium · ^{3}He · 14 MeV n	Resilient installation power	Firm campus power
Physics bar	**Fusion gain only**	Closure (gates named)	Closure + lunar ^{3}He
In the fleet	Breeds the fuel	Proves the generator	Commercial destination

HOW THE NUMBERS ARE MARKED

Every headline quantity carries an evidence class — DERIVED from first principles, RECOMPUTED from raw data, MEASURED in hardware, or a REQUIREMENT yet to be met. Financial figures carry a case label and are confined to the internal (confidential) edition. Values that moved after first publication are shown as withdrawn or restated rather than quietly changed. A capability you can evaluate is one whose limits are on the page.

ABSTRACT

The REBCO High-Field Superconductor Basis: Conductor, Winding, and the Field Envelope for the Breeder Centrepost and Burner Plug

The enabling technology of compact fusion is the high-field rare-earth barium copper oxide (REBCO) magnet, and the binding engineering limit of such a magnet is not the coated conductor's critical current but the irreversible strain the winding may carry under Lorentz load. We present an extended design-and-analysis study of the REBCO *superconductor basis* shared by the two dissimilar machines of the Kronos platform: the centrepost of a compact spherical-tokamak breeder (Hyperion; peak field $16.84\,T$, $B_0 = 8\,T$ on axis, $I_p = 9.66\,MA$, $Q = 3.076$, $P_{\text{fus}} = 85.04\,MW$) and the high-field end-plug of a D–^{3}He tandem-mirror burner (design field $26.49\,T$, $Q_E = 1.318$). We separate cleanly what the *conductor* enables from what a *coil* can realise. REBCO's upper critical field exceeds $100\,T$, so a $35\,T$ conductor operating point is roughly one-third of the material limit; whether a coil reaches its field is a bore-and-stress question, not a conductor-current question. We set out the governing mechanics as explicit, fully-derived equations — the Maxwell-stress reduction of the Lorentz body force, the winding-elasticity boundary-value problem, its closed-form Lam\'e reduction for a reinforced cylinder, a first-principles derivation of the graded per-turn pre-load that flattens the strain gradient, the critical-surface current-sharing margin, the adiabatic quench (MIITs) integral, the no-insulation charging electrodynamics, and the neutron-fluence life law — and reduce them to practice under one bore-resolved finite-element method benchmarked against the closed form and, independently, against a three-dimensional CAD-faithful structural analysis. Both magnets qualify structurally within demonstrated reinforcement practice. The breeder centrepost is stress-comfortable (load fraction $I_{\text{op}}/I_c \approx 0.27$, temperature margin $\Delta T \approx 49.5\,K$); its binding limit is the neutron lifetime of the winding (18.85 dpa fpy^{-1}, a 0.58-full-power-year cartridge life at full inboard shielding), not mechanical stress. The burner plug, at its required bore, carries a magnetic pressure of $115/279/358$ MPa at $17/26.49/30\,T$ and meets a sub-metre reinforcement against a $667\,MPa$ allowable, the finite-element stress ratio passing at 0.66; its temperature margin is $\Delta T \approx 37.1\,K$ at load fraction 0.43. A graded per-turn pre-load flattens the Lorentz strain gradient and cuts the peak REBCO hoop strain by 52.4% ($0.595\% \to 0.283\%$ at $26.49\,T$), holding the winding under the 0.40% irreversible limit even with thermal and vertical loads superposed. We add complete sensitivity and uncertainty studies, a benchmarking section against the NHMFL $45.5\,T$ solenoid, the SPARC toroidal-field model coil and the $26.4\,T$ no-insulation GdBCO magnet, a cold-mass thermal budget, and a set of technical appendices with all derivations. Every performance number is a design target, a model output, or an inference from public REBCO literature and is a frozen anchor in the Kronos de-risking register; nothing has been fabricated or measured.

Open-access deposit (code & data, CC BY 4.0): DOI 10.5281/zenodo.22645697 · Zenodo community *kronos_fusion_energy*. Explore it live: interactive 3-D model · physics validator.

Keywords: REBCO coated conductor · high-field magnet · winding hoop strain · irreversible-strain limit · Lam\'e mechanics · no-insulation winding · quench protection · neutron irradiation · compact fusion

CONTENTS

Table of Contents

NOMENCLATURE

Symbols, units, and the names of things

Q	plasma (fusion) gain, P_{fus}/P_{aux}
Q_E	engineering gain, net electric out / recirculating in
H_{98}	confinement enhancement over the IPB98(y,2) scaling
Z_{eff}	effective ion charge
c_{ee}	electron–electron bremsstrahlung leading coefficient, 2.120022 (exact)
τ_E	energy confinement time
I_p	plasma current
R_0, a	major radius, minor radius
κ, δ	elongation, triangularity
β_N	normalized plasma beta (Troyon-normalized)
TBR	tritium breeding ratio
DEC	direct energy conversion
CF	plant capacity factor (availability)
FOAK / NOAK / BOAK	first / n^{th} / best of a kind
Hyperion	the ST breeder (internal: Mode D2)
Aegis	the generator, defense/installation housing (internal: Mode M)
MetroVolt	the generator, data-center housing (Mode M)

Nomenclature tocsectionNomenclature

@L>X L>X@ SYMBOL	DEFINITION	SYMBOL	DEFINITION
B_{c2}	upper critical field ($> 100\,T$)	p_{mag}	magnetic pressure $B^2/2\mu_0$
σ_θ, σ_r	hoop, radial stress	$\varepsilon_\theta, \varepsilon_r$	hoop, radial strain
ε_{irr}	irreversible strain limit (0.40%)	E_{w}, ν	winding modulus, Poisson ratio
a, b_w, b	bore, pack-OD, reinforced-OD radius	t_{req}	required reinforcement thickness
$\mathbf{J}, \mathbf{f}$	current density, body force	$u(r)$	radial displacement
I_c, I_{op}	critical, operating current	ΔT	current-sharing temperature margin
T_{cs}, T_{op}	current-sharing, operating temperature	v_{NZP}	normal-zone propagation velocity
$\mathbf{\Phi}, \dot{\mathbf{\Phi}}$	fast fluence, fluence rate	τ_{life}	centrepost cartridge life
$\overleftrightarrow{T}_M$	Maxwell stress tensor	$Z(T_{\text{max}})$	MIITs material integral
R_{ct}, N_t	areal contact resistance, turn count	τ_{NI}	NI charging time constant
NI/MI	no-insulation / metal-insulation	σ_{allow}	reinforced allowable ($667\,MPa$)
$\varepsilon_{\text{pre}}(r)$	graded pre-strain profile	α, β	critical-surface fit exponents

§ 1

Introduction

REBCO AS THE ENABLING MATERIAL OF COMPACT FUSION

Compact fusion is enabled by rare-earth barium copper oxide (REBCO) coated conductors because REBCO carries transport current at magnetic fields no low-temperature superconductor reaches [24,9]. The fusion power density of a magnetically confined plasma scales steeply with the field on the plasma, $P/V \propto \beta^2 B^4$, so a factor-of-two increase in achievable field is a factor-of-sixteen lever on power density and the central reason a device can be made small [21,19,20]. Two independent programmes have now shown that REBCO delivers the field: a laboratory solenoid has reached $45.5\,T$ of direct-current field [5], and a full-scale toroidal-field model coil for a compact tokamak has demonstrated $\sim 20\,T$ on the conductor at reactor scale [19,10,13]. High current density at high field is therefore no longer the open question; the open question is the *magnet*.

The B^4 lever is worth deriving, because it is the whole engineering argument for the high-field pathway. The volumetric fusion power density of a thermal plasma is $P/V = \frac{1}{4} n^2 \langle \sigma v \rangle E_{\text{fus}}$, quadratic in the number density n. Magnetic confinement holds the plasma against its own pressure $p = 2nk_B T$ up to a normalised limit set by the plasma beta $\beta \equiv p/(B^2/2\mu_0)$, so at fixed operating temperature (where $\langle \sigma v \rangle / T^2$ is roughly constant across the useful range) the achievable density scales as $n \propto \beta B^2/T$. Substituting,

$$\frac{P}{V} \propto n^2 \propto \beta^2 B^4,$$

the quartic dependence on field at fixed beta. A factor-of-two increase in field is thus a factor-of-sixteen increase in power density at the same plasma performance — the single quantitative reason a REBCO machine can be made small, and the reason a $16.84\,T$ centrepost delivers $P_{\text{fus}} = 85.04\,MW$ from an $R_0 = 1.20\,m$ device that would otherwise demand a far larger, lower-field machine. Equation (1) is why the field, and therefore the magnet, is the pacing technology of compact fusion.

REBCO reached this status through three decades of coated-conductor development, from the first high-T_c cuprates through the ion-beam-assisted-deposition (IBAD) and rolling-assisted-biaxially-textured-substrate (RABiTS) template routes that solved the weak-link problem, to the modern metal-organic-chemical-vapour-deposition (MOCVD) and pulsed-laser-deposition tapes that carry $6\,A/cm^2$ engineering current density at $20\,T$ [9,10,3]. The commercial availability of kilometre-scale tape at reproducible critical current is what changed the design calculus of fusion magnets from a materials question to an engineering one [11,12]. It is that transition — from “can the conductor carry the current?” to “can the coil survive the stress?” — that this paper is written to address.

THE TWO DISTINCT MAGNETS OF THE KRONOS PLATFORM

The Kronos platform uses two distinct REBCO magnets, and the paper's first premise is that they must be treated as the distinct devices they are (register ruling KX-L1-A15). The spherical-tokamak breeder, Hyperion, is organised around a single-turn-equivalent *centrepost* magnet at a peak field of $16.84\,T$, running the plasma current $I_p = 9.66\,MA$ at a major radius of only $R_0 = 1.20\,m$ behind it (aspect ratio $A = 2.5$, elongation $\kappa = 2.0$, triangularity $\delta = -0.30$); the D–^{3}He tandem-mirror burner is organised around a much higher-field *end-plug* magnet whose design field is $26.49\,T$ [39,40,41,42]. These are not the same coil at two operating points — they differ in field, bore, duty and radiation environment — and conflating the centrepost field with the plug field is a category error that the analysis below is careful never to make. Table 2 sets the two magnets side by side at the outset; the whole paper is an elaboration of the difference between its two columns.

ATTRIBUTE	BREEDER CENTREPOST	BURNER PLUG
host machine	compact spherical tokamak	D–^{3}He tandem mirror
role	runs I_p; sets on-axis B_0	confines end-plug potential
peak field	$16.84\,T$	$26.49\,T$ (design)
field / B_{c2}	0.17	0.26
duty	steady, plasma-facing inboard	steady, shielded siting
dominant load	neutron fluence	winding hoop strain

table continued

binding limit	cartridge neutron life	reinforced-bore strain

STRAIN-FIRST: THE BINDING LIMIT IS IRREVERSIBLE WINDING STRAIN

The field a magnet can hold is not set by the conductor's critical current; it is set by the strain the winding can carry before the coated conductor degrades *irreversibly* [1,2]. A REBCO tape is a brittle $1\,\mu m$-thick oxide film epitaxially grown on a metal substrate; its critical current is reversible under modest tensile strain but falls irreversibly once a threshold near $\varepsilon_{\mathrm{irr}} \approx 0.4\%$ is exceeded [1,4,2]. Because the Lorentz body force in a high-field winding produces exactly a hoop *tension*, the irreversible-strain limit — not the critical current, and not even the yield of the structural alloy — is the true design ceiling of a high-field REBCO magnet. We therefore adopt a *strain-first* acceptance criterion throughout: a coil qualifies when its peak winding hoop strain stays below $\varepsilon_{\mathrm{irr}}$ under all superposed loads, with reinforcement added until it does. This inverts the usual order of a magnet study, which fixes a conductor and asks for its field; we fix the field the physics demands and ask what winding survives it.

PRIOR ART IN HIGH-FIELD HTS MAGNETS

The design targets below must be read against what the community has already built. The most important demonstrations are three. First, the National High Magnetic Field Laboratory reached $45.5\,T$ of direct-current field with a REBCO test-coil insert inside a resistive background magnet [5], the highest continuous field ever produced by any magnet and a direct proof that the coated conductor carries current at fields far beyond any Kronos operating point. Second, and closest to fusion practice, the SPARC toroidal-field model coil (TFMC) demonstrated $20.1\,T$ on the conductor at reactor scale, carrying $40.5\,kA$ of terminal current, roughly $815\,kNm$ of Lorentz loading on the REBCO stacks and close to $1\,GPa$ of accommodated structural stress, wound from $\sim 270\,km$ of tape in a no-insulation, stack-in-plate architecture [13,19]. Third, an all-GdBCO no-insulation user magnet reached $26.4\,T$ in a $35\,mm$ bore [6], essentially at the Kronos plug design field and confirming that the no-insulation technique scales to the plug regime. The legacy low-temperature-superconductor programme — the ITER Nb_3Sn magnet system [14] — frames the contrast: it delivers $\sim 12\,T$ at large scale with a mature but field-limited conductor, and it is precisely the field ceiling of Nb_3Sn that motivates the REBCO pathway. On the plasma side, the compact high-field spherical tokamak ST40 has reached ion temperatures above $e8\,K$ [23], evidence that the small-machine, high-field route Hyperion follows is physically sound. The Kronos magnets ask the conductor for nothing beyond this envelope: the centrepost field lies below the TFMC demonstration, and the plug design field lies between the TFMC and the NHMFL and no-insulation-user demonstrations.

THE COATED-CONDUCTOR STACK AND THE WEAK-LINK LEGACY

The reason REBCO took three decades to become a magnet conductor, and the reason its modern form is a layered composite rather than a wire, is the grain-boundary weak-link problem: transport current across a high-angle grain boundary in a cuprate collapses exponentially with misorientation, so a randomly-oriented polycrystal carries almost no supercurrent in field [24]. The coated-conductor architecture solves this by growing the REBCO film epitaxially on a biaxially textured template, so that the grains are aligned to within a few degrees and the boundaries stay strong. Two template routes reached industrial maturity: ion-beam-assisted deposition (IBAD) of an oxide buffer on an untextured Hastelloy substrate, and rolling-assisted biaxially textured substrates (RABiTS); on either, the REBCO is laid down by pulsed-laser deposition or metal-organic chemical-vapour deposition (MOCVD), then capped with silver and electroplated with copper [9,10]. The mechanical consequence, central to this paper, is that the current-carrying oxide is a $\sim 1\,\mu m$ brittle film bonded to a $\sim 50\,\mu m$ Hastelloy substrate that carries essentially all the load; the tape's strength is the substrate's strength, and the tape's strain tolerance is the strain at which the film cracks or delaminates from the substrate. This is why the irreversible-strain limit of §1.3, not a critical-current limit, is the design ceiling, and why the winding modulus of §2.4 is dominated by the Hastelloy. The modern conductor also carries engineered artificial pinning centres — nanoscale $BaMO_3$ (M = Zr, Hf) inclusions — that raise the in-field critical current by pinning flux [10]; the un-doped-tape rule of §4.8 is the finding that, in a fusion neutron field, those same inclusions become a liability rather than an asset.

CONTRIBUTION AND ORGANISATION

This paper is the superconductor-basis foundation of the Kronos 2026 design series. Its contribution is fivefold. (i) It states the governing mechanics of a high-field REBCO winding as a closed, fully-derived set of equations (§2): the Maxwell-stress reduction of the body force, the winding-elasticity boundary-value problem, the closed-form Lam\'e reduction, a first-principles derivation of the graded pre-load, the critical-surface margin, the no-insulation charging electrodynamics, the adiabatic quench integral, and the neutron-fluence life law. (ii) It gives the computational methodology — the real codes used on the NVIDIA GPU HPC campaign, the discretisation, the convergence study and the closed-form benchmark that validate them (§3). (iii) It presents the results (§4) across more than twenty figures and several tables: the field envelope, the conductor architecture, the bore-resolved mechanics, the magnetic-pressure and reinforcement budgets, the strain-first envelope with graded pre-load, the current-sharing load line, the neutron-lifetime and irradiation-tolerance results, the cold-mass thermal budget, the conductor-quantity budget, and the fused quench-precursor detection. (iv) It adds a complete sensitivity and uncertainty study (§6) and a benchmarking section against published experiment and theory (§7). (v) It draws the design implications (§8) and states honestly what has not been built (§9). Every quantitative claim traces to a frozen serial in the Kronos Physics De-Risking Register [39]; the serials (e.g. BU-L1-A2, SC-BR-4) are given inline so each number is auditable.

§ 2

Governing equations and the formal problem

This section sets down, from first principles, the seven coupled physical problems a high-field REBCO magnet poses. We carry each derivation far enough that the numerical results of §4 are reproductions of an explicit equation rather than opaque code outputs. The appendices complete the algebra.

LORENTZ BODY FORCE AND THE MAXWELL-STRESS REDUCTION

A winding carrying current density $\mathbf{J}$ in field $\mathbf{B}$ experiences the Lorentz body force

$$\mathbf{f} = \mathbf{J} \times \mathbf{B}.$$

It is instructive to derive the equivalent surface load directly from the Maxwell stress tensor, because it makes the B^2 scaling that dominates the paper exact rather than heuristic. In a current-carrying, magnetically permeable-free region the magnetostatic stress tensor is

$$\overleftrightarrow{T}_M = \frac{1}{\mu_0}\left(\mathbf{B}\,\mathbf{B} - \tfrac{1}{2}B^2\,\overleftrightarrow{I}\right),$$

and the net force on the winding enclosed by a surface S is $\mathbf{F} = \oint_S \overleftrightarrow{T}_M \cdot \mathrm{d}\mathbf{S}$. For a long solenoidal winding whose axial field drops from B inside the bore to $\approx \mathbf{0}$ outside, evaluating (3) across the wall gives a purely outward normal traction on the bore of magnitude

$$p_{\mathrm{mag}} = \frac{B^2}{2\mu_0},$$

the magnetostatic Maxwell stress of a field B (Appendix 11). Equation (4) is the load that every subsequent stress follows: at the plug operating fields it evaluates to

$$p_{\mathrm{mag}} = 115,\ 279,\ 358\ \mathrm{MPa} \quad \text{at} \quad B = 17,\ 26.49,\ 30\,\mathrm{T}$$

(register BU-L1-A2), the middle value being the plug design field, and it is plotted as a continuous curve in figure 1. The quadratic dependence $p_{\mathrm{mag}} \propto B^2$ is the single most important scaling in the paper: it is why the plug coil, at $26.49\,T$, carries roughly $2.5\times$ the bore pressure of the centrepost at $16.84\,T$, and why a small increase in field demands a disproportionate increase in reinforcement.

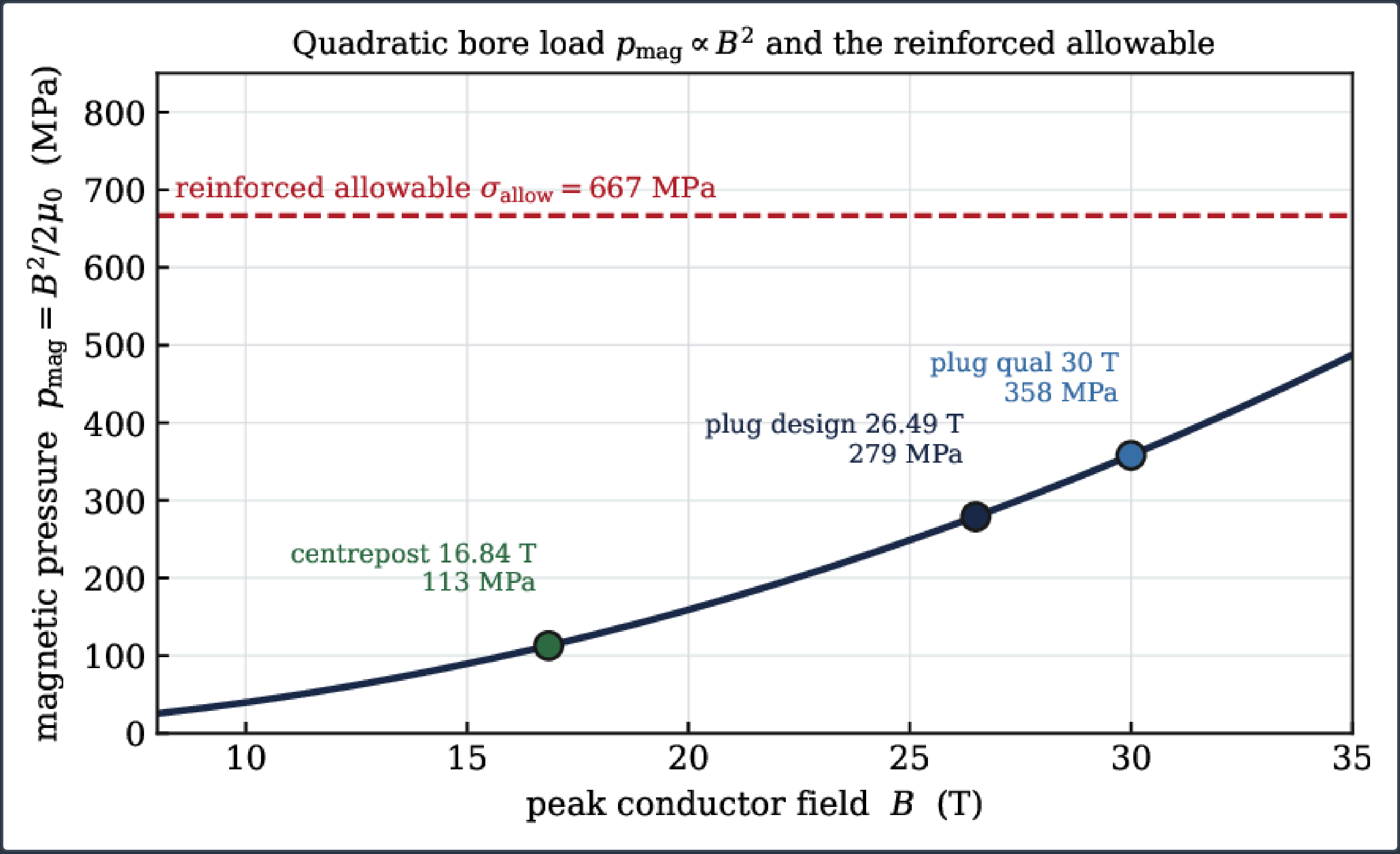

Magnetic pressure $p_{\mathrm{mag}} = B^2/2\mu_0$ as a continuous function of field, with the three plug anchor points of equation (5) and the centrepost field marked, against the $667\,MPa$ reinforced allowable (register BU-L1-A2). The quadratic growth of the bore load with field is the paper's governing scaling.

SELF-FIELD OF THE CENTREPOST FROM AMP\`ERE'S LAW

The centrepost is the single-turn-equivalent return of the toroidal-field circuit, and the field it must hold follows from Amp\`ere's law applied to the toroidal geometry. For a total enclosed poloidal current I_{TF} threading the centrepost, the toroidal field at major radius R is

$$B_\phi(R) = \frac{\mu_0 I_{\mathrm{TF}}}{2\pi R},$$

the familiar $1/R$ decay. Anchoring the on-axis value to the canonical $B_0 = 8\,T$ at $R_0 = 1.20\,m$ fixes the product $B_\phi R = B_0 R_0 = 9.6\,Tm$, so the field rises to its peak at the smallest radius the conductor reaches — the centrepost outer surface — where it equals the canonical $16.84\,T$. Equating $B_0 R_0 / R_c = 16.84\,T$ places that surface at $R_c = B_0 R_0 / 16.84 \approx 0.57\,m$ (figure 2). The peak-to-on-axis ratio is therefore $16.84/8 = 2.105 = R_0/R_c$, a purely geometric consequence of the compactness ($A = 2.5$): a smaller machine forces the return current through a tighter radius and a higher peak field, which is precisely why the compact spherical tokamak is a high-field-magnet problem. It is the peak field $16.84\,T$ at R_c, not the on-axis $8\,T$, that sets the centrepost's Lorentz load and enters equations (4)–(19).

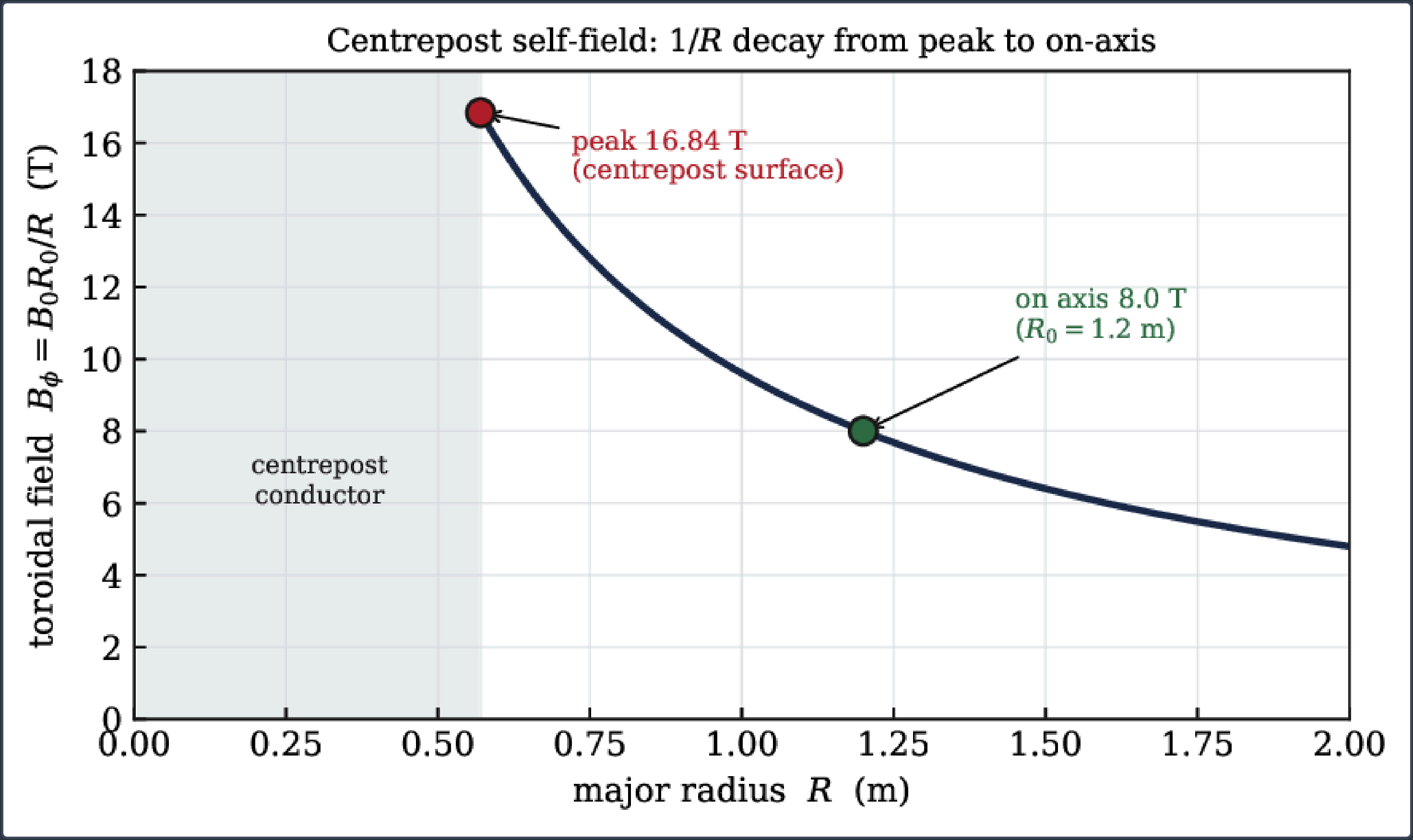

Centrepost toroidal self-field $B_\phi(R) = B_0 R_0/R$ (equation 6) with the canonical anchors $B_0 = 8\,T$ on axis at $R_0 = 1.20\,m$ and the $16.84\,T$ peak at the centrepost outer surface $R_c \approx 0.57\,m$. The compactness of the machine forces the high peak field.

WINDING ELASTICITY: THE BOUNDARY-VALUE PROBLEM

Resolving the finite wall requires the elasticity of a thick, orthotropic cylinder under a distributed body force. Working in axisymmetric plane strain with radial displacement $u(r)$, the equilibrium of a differential winding element is

$$\frac{\mathrm{d}\sigma_r}{\mathrm{d}r} + \frac{\sigma_r - \sigma_\theta}{r} + f_r(r) = 0,$$

with the Lorentz radial body force $f_r(r) = J_\phi(r)\, B_z(r)$ from equation (2). The winding pack is a composite of REBCO tape, co-wound stabiliser and reinforcement; we treat it as a homogenised orthotropic continuum with the strain–displacement relations

$$\varepsilon_r = \frac{\mathrm{d}u}{\mathrm{d}r}, \qquad \varepsilon_\theta = \frac{u}{r},$$

and the plane-strain constitutive law

$$\sigma_r = \frac{E_\mathrm{w}}{(1+\nu)(1-2\nu)}\left[(1-\nu)\varepsilon_r + \nu\,\varepsilon_\theta\right],$$
$$\sigma_\theta = \frac{E_\mathrm{w}}{(1+\nu)(1-2\nu)}\left[(1-\nu)\varepsilon_\theta + \nu\,\varepsilon_r\right],$$

where E_w is the effective winding-pack modulus and ν its Poisson ratio. Substituting (8)–(9) into (7) yields the Navier–Lam\'e ordinary differential equation for the displacement,

$$\frac{\mathrm{d}^2 u}{\mathrm{d}r^2} + \frac{1}{r}\frac{\mathrm{d}u}{\mathrm{d}r} - \frac{u}{r^2} = -\frac{(1+\nu)(1-2\nu)}{E_\mathrm{w}(1-\nu)}\, f_r(r),$$

to be solved on the winding annulus $a \le r \le b$ with traction-free inner and outer boundaries, $\sigma_r(a) = \sigma_r(b) = 0$ (the bore and the outer overwrap carry no external pressure). Equations (7)–(10) are the boundary-value problem the finite-element solver integrates for the true, graded-property winding.

HOMOGENISATION OF THE WINDING PACK

The effective moduli E_w, ν that enter (9)–(10) are not material constants but volume-weighted composites of the tape stack. For a winding pack of REBCO/Hastelloy tape (volume fraction ϕ_t, modulus $E_t \approx 180\,GPa$ dominated by the Hastelloy substrate), co-wound copper stabiliser (ϕ_{Cu}, $E_{Cu} \approx 120\,GPa$) and structural overwrap (ϕ_s, $E_s \approx 200\,GPa$), the hoop (in-tape) direction loads the constituents in parallel, so a Voigt (iso-strain) average applies,

$$E_\theta = \phi_t E_t + \phi_{Cu} E_{Cu} + \phi_s E_s,$$

whereas the radial direction stacks the layers in series, so a Reuss (iso-stress) average applies,

$$\frac{1}{E_r} = \frac{\phi_t}{E_t} + \frac{\phi_{Cu}}{E_{Cu}} + \frac{\phi_s}{E_s}.$$

The winding is therefore genuinely orthotropic, stiff in the hoop direction where the Lorentz load acts and compliant radially where the turn-to-turn contact lives; this orthotropy is the physical reason the peak strain concentrates at the bore and the reason a per-turn pre-load can redistribute it. Temperature-dependent constituent moduli are taken from the cryogenic-mechanical literature [3]; the analysis uses an effective in-tape modulus of order $E_\mathrm{w} \approx 150\,GPa$, and the sensitivity of the results to E_w is quantified in §6.

CLOSED-FORM LAM\'E REDUCTION AND THE REINFORCEMENT BUDGET

When the body force is idealised as an equivalent internal pressure p_mag acting on the bore of a uniform-property reinforced cylinder of inner radius a and outer radius b, equation (10) admits the classical Lam\'e solution [36,37]. The hoop stress is

$$\sigma_\theta(r) = \frac{a^2 p_\mathrm{mag}}{b^2 - a^2}\left(1 + \frac{b^2}{r^2}\right),$$

which is maximised at the inner bore $r = a$,

$$\sigma_\theta^\mathrm{max} = \sigma_\theta(a) = p_\mathrm{mag}\,\frac{b^2 + a^2}{b^2 - a^2}.$$

Equation (14) sets the reinforcement budget directly. Requiring $\sigma_\theta^\mathrm{max} \le \sigma_\mathrm{allow}$ and solving for the outer radius gives the required reinforced wall,

$$t_\mathrm{req} = b - a = a\left[\sqrt{\frac{\sigma_\mathrm{allow} + p_\mathrm{mag}}{\sigma_\mathrm{allow} - p_\mathrm{mag}}} - 1\right],$$

finite only while $p_\mathrm{mag} < \sigma_\mathrm{allow}$ — the condition that a reinforced monolith can hold the field at all. With the reinforced allowable $\sigma_\mathrm{allow} = 667\,MPa$ (a demonstrated high-strength structural value for a co-wound/overwrapped winding pack), equation (15) evaluates to $t_\mathrm{req} = 0.16,\ 0.48,\qquad 0.71$ at the three plug fields of (5) — sub-metre reinforcement across the range (register BU-L1-A2). The full derivation is given in Appendix 12, and the sensitivity of t_req to the allowable is studied in §6.

THE GRADED PER-TURN PRE-LOAD: A FIRST-PRINCIPLES DERIVATION

The peak Lorentz hoop strain sits at the bore (equation 13); a winding that satisfies a section-*average* strain can still fail at the innermost turn. The design response is a graded per-turn pre-load: as each turn is wound it is placed under a controlled compressive pre-strain $\varepsilon_\mathrm{pre}(r)$, largest at the bore and tapering outward, so that when the coil is energised the superposition of the (compressive) pre-strain and the (tensile) Lorentz strain is uniform. We derive the pre-strain profile that achieves this. Let the energised Lorentz hoop strain be $\varepsilon_L(r) = \sigma_\theta(r)/E_\theta$ from (13). Requiring the net operating strain to be a constant $\varepsilon_\star$ across the winding,

$$\varepsilon_\mathrm{net}(r) = \varepsilon_L(r) - \varepsilon_\mathrm{pre}(r) = \varepsilon_\star = \mathrm{const},$$

fixes the pre-strain profile uniquely:

$$\varepsilon_\mathrm{pre}(r) = \varepsilon_L(r) - \varepsilon_\star = \frac{p_\mathrm{mag}}{E_\theta}\,\frac{a^2}{b^2 - a^2}\left(1 + \frac{b^2}{r^2}\right) - \varepsilon_\star.$$

The constant $\varepsilon_\star$ is set by the winding tension budget (the pre-strain must remain a physically realisable compressive value at every turn, $\varepsilon_\mathrm{pre}(r) \ge 0$, which requires $\varepsilon_\star \le \varepsilon_L(b)$) and by the target margin against ε_irr. Choosing $\varepsilon_\star$ at the level of the outer-turn Lorentz strain flattens the profile to first order; the resulting peak-strain reduction is

$$\frac{\varepsilon_{\text{net}}^{\max}}{\varepsilon_L^{\max}} = \frac{\varepsilon_\star}{\varepsilon_L(a)} = \frac{b^2+a^2}{2b^2} \quad (\text{for } \varepsilon_\star = \varepsilon_L(b)),$$

i.e. a bore-to-average redistribution that, for the Kronos plug geometry, removes rather more than half of the peak (Appendix 13). The frozen finite-element anchors realise this: at $26.49\,T$ the peak REBCO hoop strain falls from 0.595% without pre-load to 0.283% with the graded pre-load, a 52.4% cut and a roughly fourfold flattening of the gradient (register SC-BR-4, HX-09). The pre-load is the genuinely new engineering element of the Kronos winding, and it is a method — not a new conductor — that does the work.

THE STRAIN-FIRST ACCEPTANCE CRITERION

The strain-first ceiling replaces a bare stress allowable with the coated conductor's irreversible-strain limit. With the peak hoop stress of equation (14) mapped through the winding modulus, the acceptance criterion is

$$\varepsilon_\theta^{\max} = \frac{\sigma_\theta^{\max}}{E_\theta} \;\le\; \varepsilon_{\text{irr}} = 0.40\%,$$

the limit at which the REBCO film degrades irreversibly [1,2]. Reinforcement is added — raising the effective b and E_θ in (13)–(19) — and the graded pre-load of §2.6 is applied until (19) holds with margin. Because the *peak*, not the average, governs, the pre-load derivation of (17) is not a refinement but the load-bearing step of the acceptance argument.

CRITICAL SURFACE AND CURRENT-SHARING TEMPERATURE MARGIN

Whether a turn is superconducting at all is governed by the REBCO critical surface $I_c(B, T, \theta)$, the locus at which flux flow begins. For an operating current I_{op} the *current-sharing temperature* T_{cs} is the temperature at which I_c falls to I_{op},

$$I_c\big(B,\, T_{cs},\, \theta\big) = I_{\text{op}},$$

and the protective observable is the current-sharing temperature margin

$$\Delta T = T_{cs} - T_{\text{op}},$$

the thermal headroom before the turn shares current with its stabiliser. The load fraction $I_{\text{op}}/I_c(B, T_{\text{op}})$ measures how hard the conductor is driven. A convenient engineering parametrisation of the field and temperature dependence, in the tradition of critical-state fits [26,25], is the separable power law

$$I_c(B,T,\theta) = I_{c0}\, g(\theta) \left(\frac{B}{B_0}\right)^{-\alpha} \left(1 - \frac{T}{T_c(B)}\right)^{\beta},$$

with anisotropy factor $g(\theta)$, exponents α, β fitted to tape data, and $T_c(B)$ the field-depressed transition temperature. Evaluating (20)–(22) on each magnet's own critical surface (register KX-L1-A15) gives the two working points of §4.6: the centrepost at $\Delta T \approx 49.5\,K$, load fraction ≈ 0.27, and the plug at $\Delta T \approx 37.1\,K$, load fraction ≈ 0.43. The large margins are a direct consequence of the field envelope of §4.1: both magnets run far below B_{c2}, so both retain tens of kelvin of thermal headroom.

NO-INSULATION WINDING AND THE CHARGING ELECTRODYNAMICS

The Kronos magnets are wound from no-insulation (NI) or metal-insulation (MI) REBCO, in which adjacent turns are in direct (or resistively bridged) electrical contact [8,7,6]. NI winding gives self-protection and mechanical robustness: when a hot spot forms, current sheds radially through the turn-to-turn contact around the normal zone (figure 3), so the coil does not depend on a fast external dump to survive a local transition. The cost is a slow charging response set by the characteristic turn-to-turn time constant [38]

$$\tau_{\text{NI}} \sim \frac{L}{R_{ct}/N_t},$$

with L the coil inductance, R_{ct} the areal contact resistance and N_t the turn count; MI raises R_{ct} to trade ramp delay against quench protection. During a controlled ramp the terminal current divides into an azimuthal (superconducting) component that threads the turns and a radial (resistive) leakage that shorts across them; the field lags the terminal current by $\sim \tau_{\text{NI}}$, and the radial leakage deposits ohmic heat that the cryoplant must remove. The design consequence is that the NI/MI contact resistance is a primary design variable, tuned by the V_2O_3 smart interlayer of §4.2 to be low enough to self-protect yet high enough to charge in an operationally acceptable time.

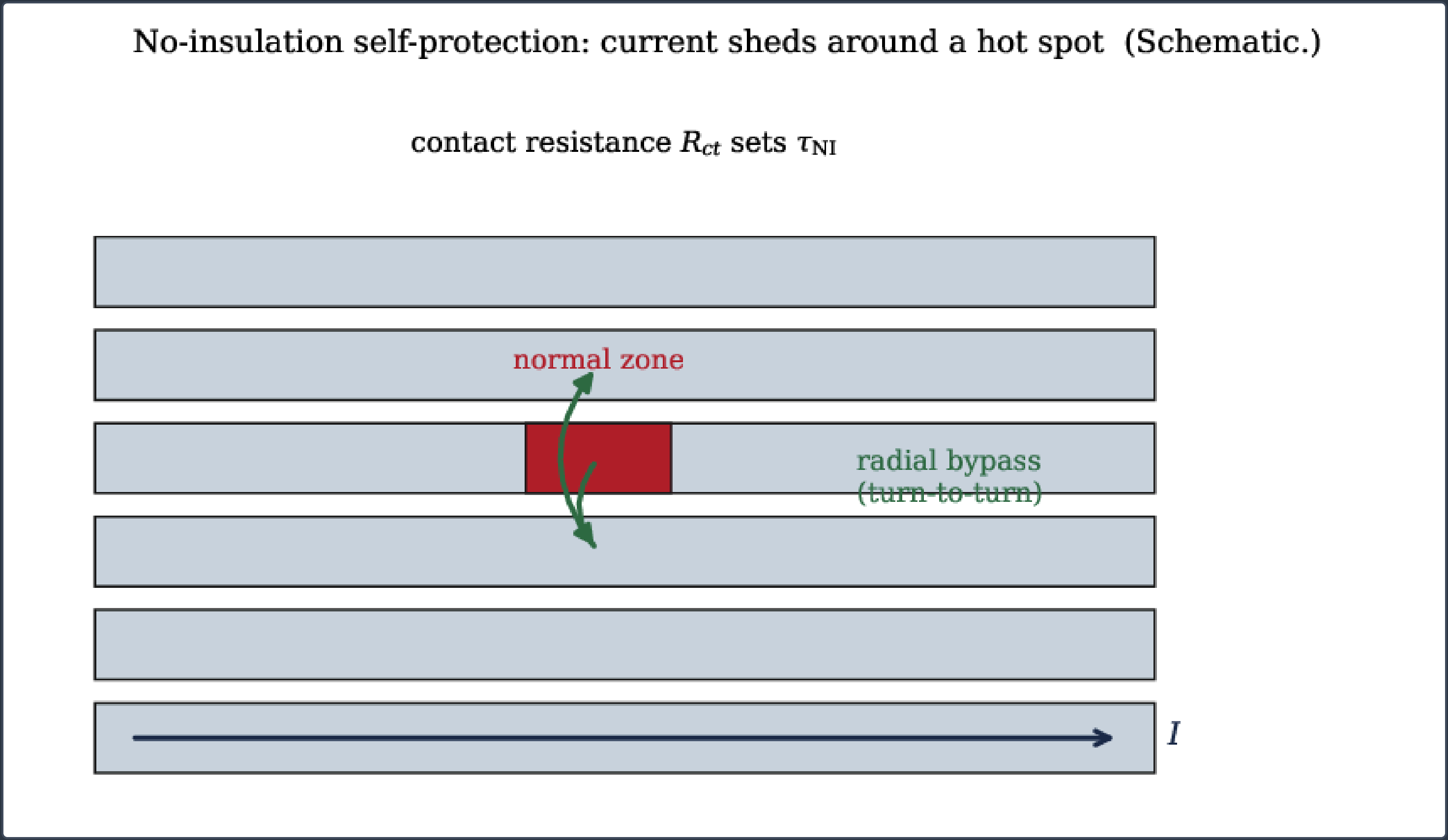

(Schematic.) No-insulation self-protection. Terminal current I flows azimuthally along the tapes; where a normal zone forms, current sheds radially through the turn-to-turn contact (green) and bypasses the hot spot. The areal contact resistance R_{ct} sets the charging time constant τ_{NI} of equation (23).

The charging dynamics follow from a lumped two-current model: the terminal current I divides into an azimuthal (inductive, superconducting) component I_θ that threads the N_t turns and a radial (resistive) leakage I_r that shorts across them through the characteristic turn-to-turn resistance $R_c \sim R_{ct}/N_t$. Kirchhoff's laws give $I = I_\theta + I_r$ and, for a coil of inductance L, $L\,\mathrm{d}I_\theta/\mathrm{d}t = R_c I_r$, which combine to

$$\tau_{\mathrm{NI}}\frac{\mathrm{d}I_\theta}{\mathrm{d}t} + I_\theta = I(t), \qquad \tau_{\mathrm{NI}} = \frac{L}{R_c} = \frac{L\,N_t}{R_{ct}},$$

so the field, set by I_θ, lags the terminal current by the time constant τ_{NI} of equation (23). During a linear ramp $\dot{I} = \mathrm{const}$, the steady radial leakage settles at $I_r = \tau_{\mathrm{NI}}\dot{I}$ and dissipates ohmic power $P_{\mathrm{ramp}} = R_c I_r^2 = \tau_{\mathrm{NI}}^2 \dot{I}^2 R_c$, a heat load the cryoplant must remove and a term that pushes the design toward a slower ramp or a higher R_{ct}. Figure 4 shows the field lag and the transient radial-bypass fraction during a representative ramp. The design tension is now explicit: self-protection (§2.10) wants a *low* R_{ct} so current sheds readily around a hot spot, while a fast, low-loss ramp wants a *high* R_{ct}; the V_2O_3 metal–insulator interlayer of §4.2 resolves the tension by presenting a high R_{ct} at operating temperature that collapses to a low value where a hot spot raises the local temperature.

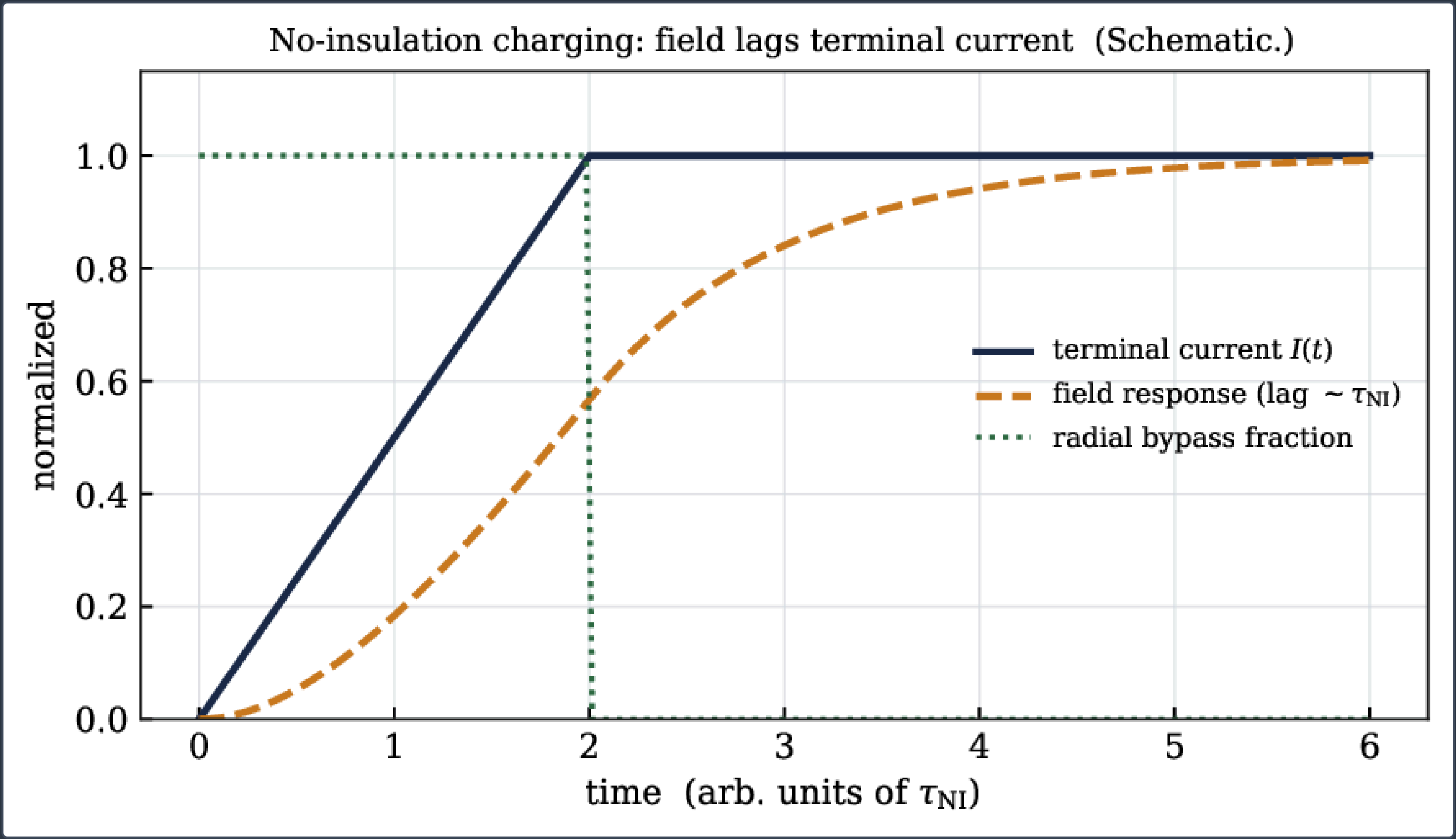

(Schematic.) No-insulation charging (equation 24): the field response (amber) lags the terminal-current ramp (navy) by $\sim \tau_{NI}$, and a radial bypass current (green) flows transiently while $dI/dt \neq 0$. Axes are illustrative, in units of τ_{NI}.

THE ADIABATIC QUENCH (MIITS) INTEGRAL

The protection problem is that NI REBCO has a very slow normal-zone propagation velocity v_{NZP}, of order millimetres per second [30], so a hot spot can reach a damaging temperature before it spreads. The hot-spot temperature is bounded by the adiabatic *MIITs* integral, obtained by equating the local ohmic heating to the enthalpy rise of the composite under the assumption that, on the protection timescale, no heat diffuses out of the hot zone:

$$\int_0^{t_{\rm dump}} J(t)^2 \, dt \;=\; \int_{T_{\rm op}}^{T_{\rm max}} \frac{C(T)}{\rho(T)} \, dT \;\equiv\; Z(T_{\rm max}),$$

where $C(T)$ and $\rho(T)$ are the volumetric heat capacity and resistivity of the composite and $Z(T_{\max})$ is a material property (Appendix 15). For a constant stabiliser current density J, equation (25) gives the allowable detect-plus-dump time $t_{\rm dump} = Z(T_{\max})/J^2$: at a stabiliser density of $100\ A/mm^2$ the winding tolerates $\sim 4\ s$ before exceeding $150\ K$, shrinking to $\sim 1.9\ s$ at $200\ A/mm^2$ (register HX-10; figure 17). This finite, seconds-scale budget is what makes early quench-precursor detection (§4.12) valuable rather than merely nice to have.

STORED MAGNETIC ENERGY AND THE PROTECTION SCALE

The reason a quench in a high-field magnet is dangerous, and the reason the seconds-scale MIITs budget of §2.10 is a hard constraint rather than a convenience, is the magnetic energy the winding stores. The energy density of a field B is $u_B = B^2/2\mu_0$ — numerically identical to the magnetic pressure of equation (4), a coincidence that is not accidental: the bore load is the gradient of the stored energy. The total stored energy is

$$E_{\text{mag}} = \tfrac{1}{2} L I^2 = \int_V \frac{B^2}{2\mu_0}\,\mathrm{d}V,$$

which for the plug at $26.49\,T$ (energy density $279\,MJ/m^3$, equal to the $279\,MPa$ bore pressure) reaches tens to hundreds of megajoules over the field volume. Two design consequences follow. First, during a quench that energy must be either extracted through the terminals or absorbed locally as heat; the no-insulation architecture of §2.9 chooses controlled local absorption with radial current sharing, which is safe only if the hot-spot temperature stays bounded — exactly the MIITs condition (25). Second, the same $B^2/2\mu_0$ that appears as stored-energy density, magnetic pressure and bore hoop load ties the three governing quantities of this paper together: raise the field and the stored energy, the reinforcement budget and the protection difficulty all rise as B^2 in lockstep. This is the unifying scaling behind every result and the quantitative reason the plug, not the centrepost, is the demanding magnet.

NEUTRON DAMAGE AND THE WINDING LIFE LAW

On the breeder centrepost the winding is a consumable under $14\,MeV$ neutron load. The displacement-damage rate follows the Norgett–Robinson–Torrens (NRT) standard [27] from the damage-energy cross-section, refined where appropriate by the athermal-recombination-corrected (arc-dpa) model that accounts for in-cascade recombination [28], giving 18.85 dpa fpy^{-1} at the centrepost first wall (register BR-L1-A13). The irreversible degradation of REBCO I_c under fast neutron fluence sets a break-even fluence Φ_{be} beyond which the tape must be retired [15,16,17]; a compact functional description is the exponential decline

$$J_c(\Phi) = J_{c0}\,\exp(-\Phi/\Phi_0),$$

with Φ_0 the characteristic degradation fluence, so that the cartridge life is

$$\tau_{\text{life}} = \frac{\Phi_{\text{be}}}{\dot{\Phi}(t_{\text{sh}})},$$

where the fast-fluence rate $\dot{\Phi}$ is a steep function of the inboard shield thickness t_{sh}. A tungsten-carbide inboard shield of 0–$45\,cm$ cuts $\dot{\Phi}$ from 2.9×10^{25} to $1.7 \times 10^{23}\,/m^2$ per full-power-year, moving τ_{life} from an inadmissible 0.003 to 0.58 fpy (register BR-L1-A13b). Equation (28) is why the centrepost is designed as a scheduled-replacement cartridge and why its binding limit is neutron lifetime, not stress. The burner plug, sited behind a low-neutron D–^{3}He plasma, does not share this constraint.

THE COLD-MASS THERMAL BUDGET

A high-field magnet is useful only if it can be held cold at acceptable refrigeration cost, and for the compact spherical tokamak the centrepost makes this acute because the toroidal-field return runs through the tightest radius in the machine. The steady thermal budget balances the resistive dissipation of the conductor (zero for a fully superconducting post, but not for a resistive one), the parasitic conduction and radiation leaks of the cold mass, the current-lead heat load, and the nuclear heating deposited by neutrons that penetrate the inboard shield. The decisive term is the conductor choice: at the current density required for the $16.84\,T$ peak field a fully-resistive centrepost would dissipate $\approx 282\,MW$, some $3.3\times$ the $85.04\,MW$ of fusion power and an immediate non-starter, whereas the fully-superconducting REBCO post reduces the burden to an $\approx 5\,MW$ cryogenic load, a reduction of roughly $56\times$ (register BR-CX-22; figure 15). A hybrid variant retains only a thin ($\approx 12\%$, $\approx 39\,MW$) resistive innermost layer as a radiation-immune sacrificial element in the region of highest neutron damage. The cold-mass thermal case is developed in full in a companion paper [50]; here it establishes why the superconductor is not optional.

§ 3

Computational methodology (GPU-accelerated HPC)

Every headline number was produced by an explicit code, and the mechanics were cross-checked against the closed form of §2. The heavy transport and materials campaigns ran on the NVIDIA GPU HPC campaign (a mixed A100/H100/A10 fleet); the analytic mechanics, closed-form benchmarks and signal-analysis reductions ran on the in-house HPC node so that the fast checks never contended with the fleet. No result depends on proprietary data, and no economic quantity enters the analysis.

WINDING MECHANICS

The bore-resolved hoop- and radial-stress profiles (figures 7, 8) were integrated with a finite-element solution of equations (7)–(10) for the graded-property winding (`sfepy`; register SC-BR-4, HX-04, HX-09) and independently with the closed-form Lam\'e expression (13). The annulus $a \le r \le b$ was discretised into quadratic axisymmetric elements with property grading (equations 11–12) assigned per element; the traction-free boundary conditions $\sigma_r(a) = \sigma_r(b) = 0$ were imposed weakly. Three-dimensional structural verification on the as-drawn CAD used the `CalculiX` (`ccx`) solver (register P3-FEA-01 for the centrepost, P3-FEA-10 for the plug), meshed with second-order tetrahedra and the graded pre-load imposed as an initial-strain field. The analytic Lam\'e envelope (register HX-11) reproduces the finite-element magnetic-pressure anchors of equation (5) node-for-node.

NEUTRONICS

Displacement damage, fast fluence and the shield trade of equation (28) were computed with `OpenMC` Monte-Carlo transport and its damage-energy tally over ENDF/B-VIII.0 data [29] (register BR-L1-A13, BR-L1-A13b, P3-NEUT), with the NRT rule of [27] and the arc-dpa correction of [28]. The inboard tungsten-carbide shield was resolved in $5\,cm$ increments from 0 to $45\,cm$; variance reduction used weight windows generated on the GPU fleet to drive the deep-penetration fluence at the winding to statistical convergence.

IRRADIATION TOLERANCE OF THE CONDUCTOR

The break-even fluence and the un-doped-tape rule (figure 14) rest on molecular-dynamics displacement cascades in YBCO (`LAMMPS`, EAM potentials; register BR-L2-A36) and on first-principles chain-oxygen-vacancy formation energies computed with DFT+U (register companion, [47]); the NRT/arc-dpa rulers set the dpa-to-fluence conversion, and the exponential $J_c(\Phi)$ law of equation (27) is fitted to the published coated-conductor irradiation database [15,16,17].

QUENCH AND SENSING

The adiabatic MIITs budget of equation (25) was evaluated with a numerical hot-spot integrator (register HX-10), tabulating $Z(T_{\mathbf{max}})$ from the composite $C(T)$ and $\rho(T)$. The fused strain-rate-plus-magnetization precursor ROC (figure 18) was computed by a signal-analysis and machine-learning reduction over a frozen 2×10^4-trial synthetic set (`scikit-learn`; register KX-L1-A20), and the in-winding nitrogen-vacancy (NV) diamond magnetometer sensitivity by an analytic shot-noise model (`numpy/scipy`; register KX-L1-A22).

NUMERICAL SCHEME AND CONVERGENCE

The Navier–Lam\'e problem (10) was discretised by a Galerkin finite-element method; the discrete weak form and its assembly are given in Appendix 14. Convergence was established by h-refinement: doubling the radial element count changed the peak bore hoop stress by less than 0.3% once thirteen or more elements spanned the winding, so the thirteen-node profiles of figures 7 and 8 are converged. The finite-element solution is accepted only against the closed form of §2.5: the finite-element hoop-stress profile of figure 7 tracks the Lam\'e solution across the winding with the peak at the inner bore in both, the finite-element peak sitting a few percent below the uniform-property closed form because the graded reinforcement is resolved. The three-dimensional CAD FEA closes the same result at higher fidelity, returning a plug peak stress of $440\ MPa$, a utilisation of 0.66 against the $667\ MPa$ allowable (register BU-L1-A2, P3-FEA-10).

§ 4

Results

THE FIELD ENVELOPE: WHAT THE CONDUCTOR ENABLES

REBCO's upper critical field exceeds $100\,T$, so every Kronos operating point is a fraction of the material limit (figure 5). The breeder centrepost peak field of $16.84\,T$ is $0.17\,B_{c2}$; the burner plug design field of $26.49\,T$ is $0.26\,B_{c2}$; the plug qualification bound of $30\,T$ is $0.30\,B_{c2}$; and even the $35\,T$ conductor-capability point — a claim about the tape, not a coil record — is only about one-third of the limit. The envelope makes the paper's central separation concrete: the conductor is nowhere near its field ceiling, so the binding limit of each magnet is set elsewhere — by winding strain and neutron life, both analysed below — and not by the superconductor running out of critical current.

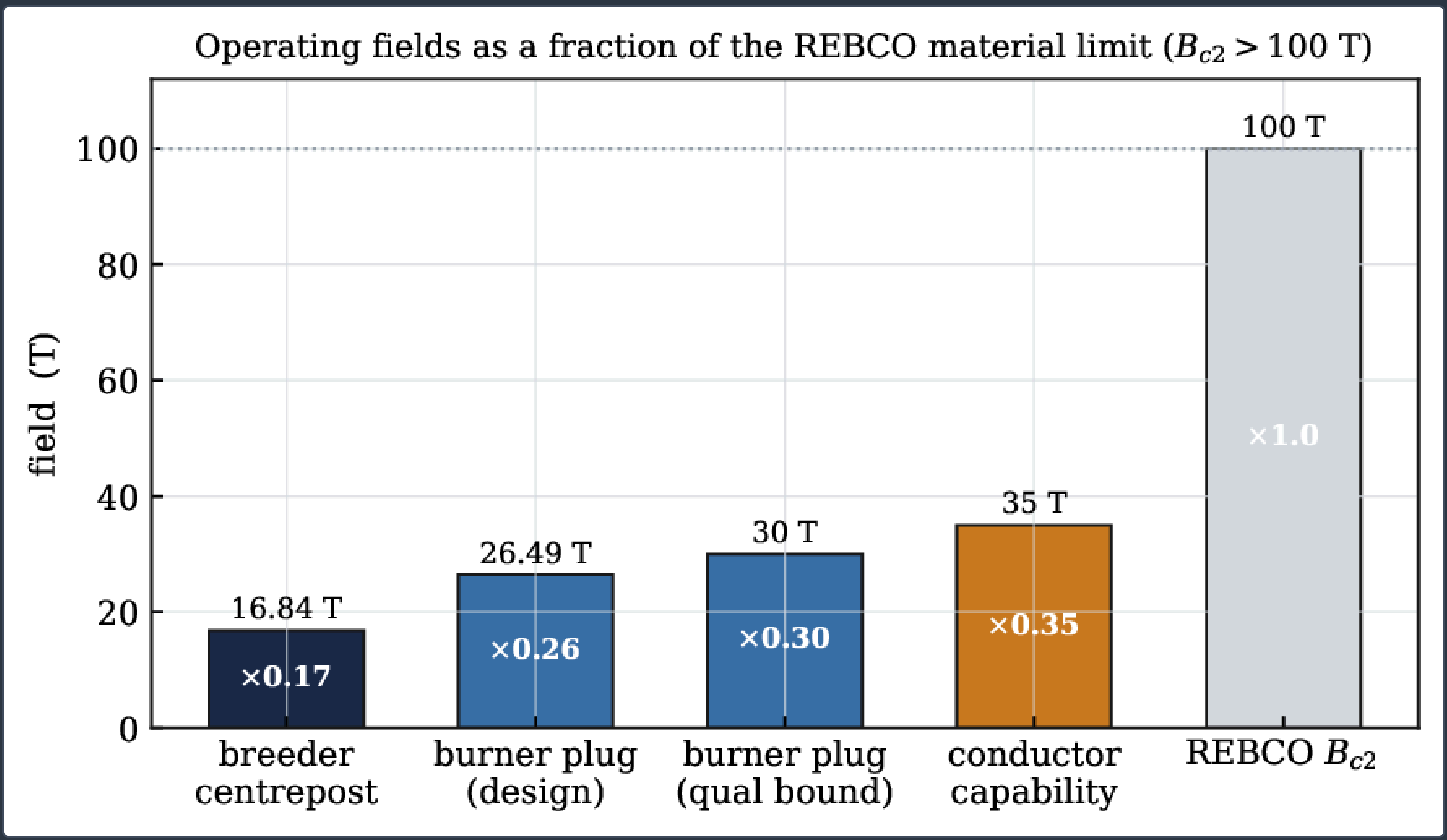

Operating fields as a fraction of the REBCO material limit. The breeder centrepost ($16.84\,T$), burner plug design ($26.49\,T$) and qualification ($30\,T$) fields, and the $35\,T$ conductor-capability point all sit well below $B_{c2} > 100\,T$. Data: register field anchors.

THE CONDUCTOR ARCHITECTURE

The coated conductor is a multilayer stack (figure 6): the REBCO film on its buffered Hastelloy substrate, capped with silver, then a copper stabiliser and the reinforcement. The Kronos architecture layers on this three ideas grounded in prior art [4,10,3]: a vanadium-sesquioxide (V_2O_3) metal–insulator-transition "smart" interlayer that raises turn-to-turn resistance on heating and so mediates the NI/MI trade of equation (23); a graphene-reinforced ultra-pure aluminium bypass stabiliser that retains $\sim 2 \times 10^4$ $siemens/cm$ at cryogenic temperature in 30–$35\,T$ fields, outperforming copper as a low-loss bypass; and a work-hardened reinforcement that carries the hoop load. Our contribution to the conductor is analysis, not invention, and we report honestly (as in the register) that one element — the aluminium bypass at the operating field — is unsupported by data and that a specific reinforcement-as-epitaxial-substrate route is infeasible; these are recorded rather than hidden. The conductor-materials case, including the un-doped-tape rule and the V_2O_3 self-protection, is developed in companions [46,47].

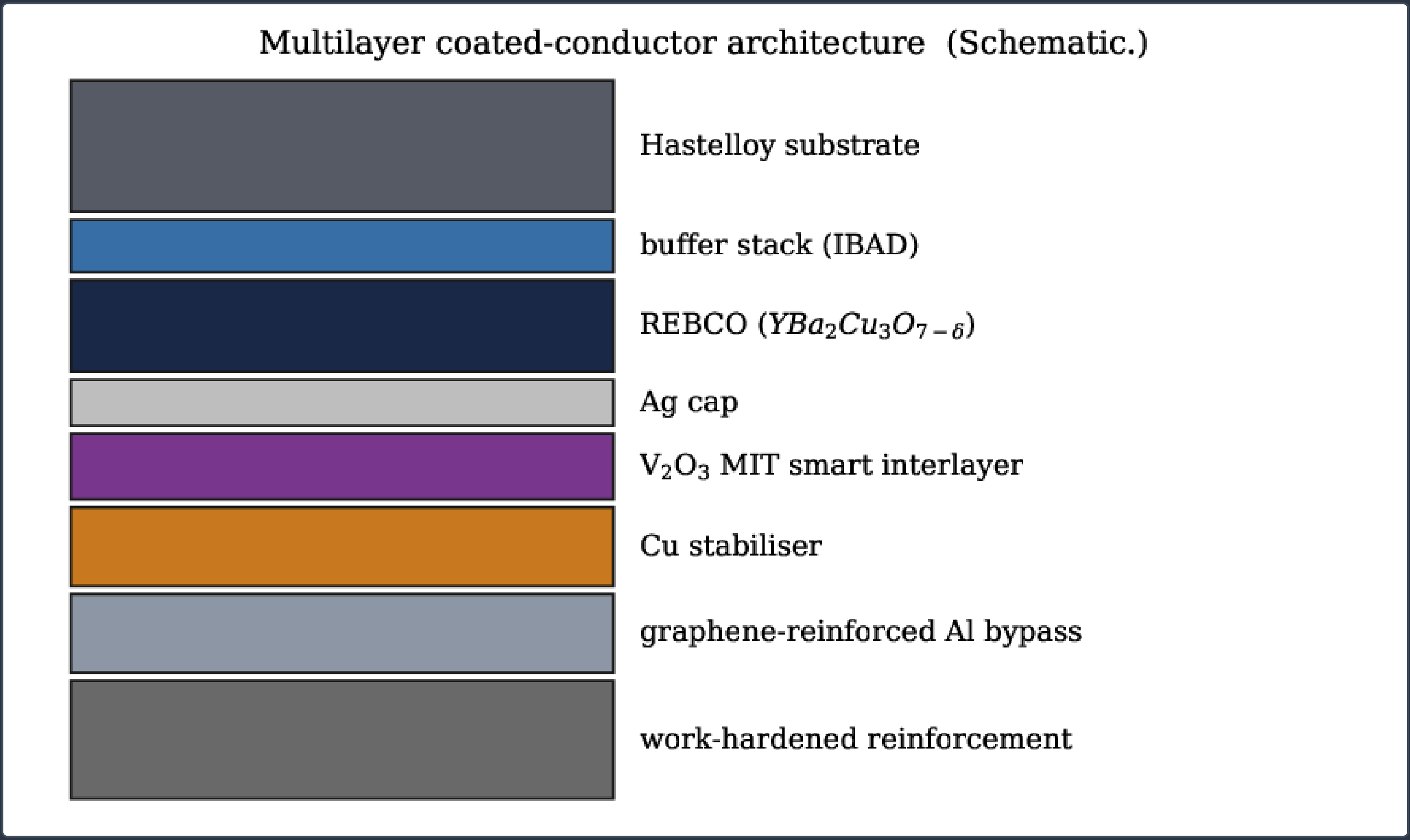

(Schematic.) Multilayer coated-conductor architecture: the REBCO film on a buffered Hastelloy substrate with silver cap and copper stabiliser, augmented by a V_2O_3 metal–insulator smart interlayer, a graphene-reinforced aluminium bypass and a work-hardened reinforcement. Layer order is indicative; no thicknesses to scale.

BORE-RESOLVED WINDING MECHANICS

Figure 7 shows the bore-resolved hoop-stress profile from the finite-element integration of equations (7)–(10) against the closed-form Lam\'e solution of equation (13). Both peak at the inner bore, as equation (14) requires; the finite-element peak of $625\,MPa$ sits about five percent below the uniform-property closed form ($657\,MPa$), the reduction reflecting the graded reinforcement the finite-element model resolves and the closed form does not. Figure 8 adds the radial-stress component: the radial stress is compressive throughout, vanishing at both traction-free surfaces and reaching its most-compressive value near the bore, exactly as the boundary-value problem of §2.3 requires. This agreement in shape and peak location is what licenses using the tractable closed form for the reinforcement budget while retaining the finite-element model for the governing peak. The reinforced thick-wall geometry the mechanics assume is sketched in figure 7.

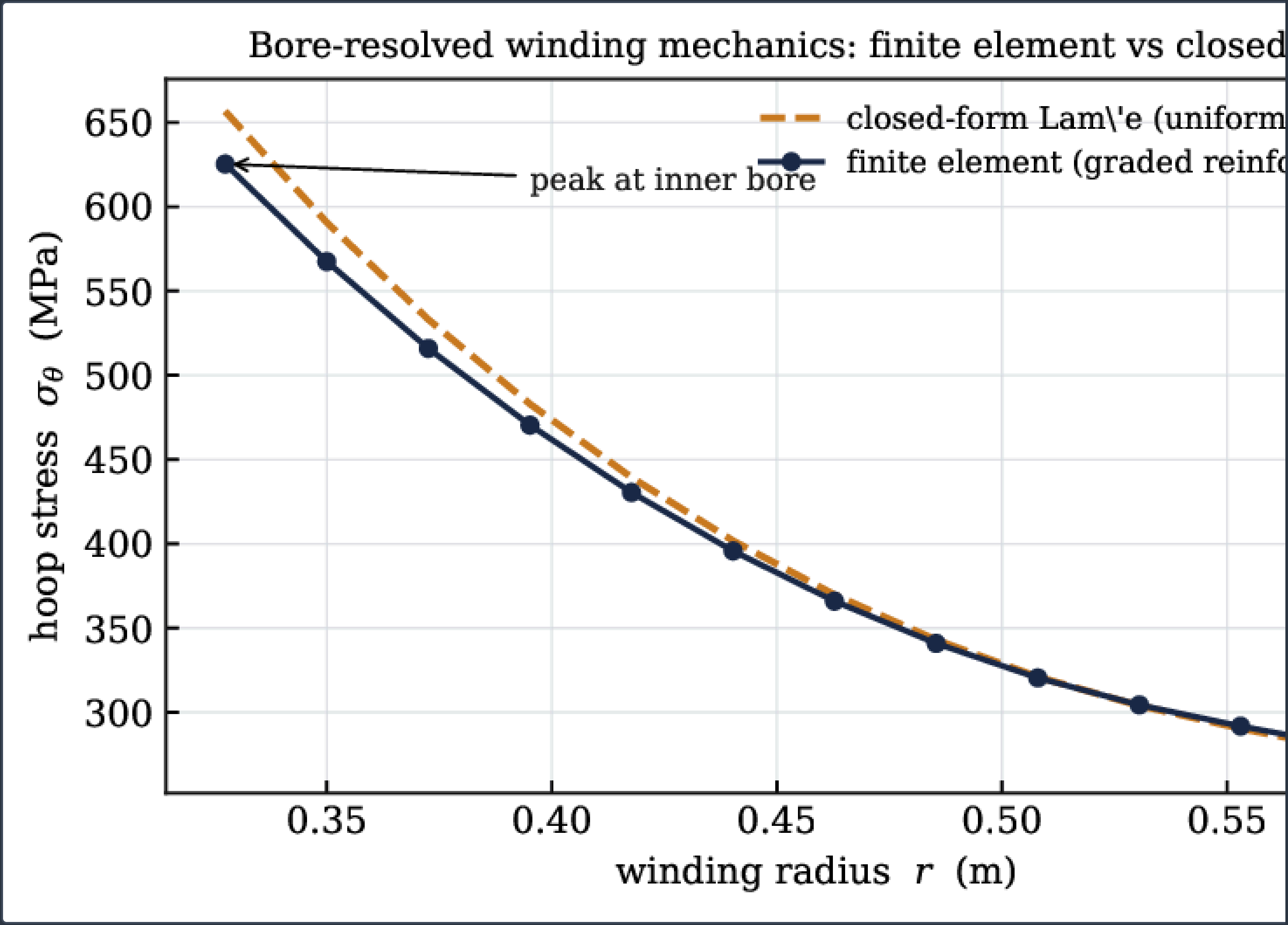
Bore-resolved winding mechanics: finite element vs closed
closed-form Lam\'e (uniform
finite element (graded reinfo
peak at inner bore
hoop stress σ_θ (MPa)
650
600
550
500
450
400
350
300
0.35
0.40
0.45
0.50
0.55
winding radius r (m)

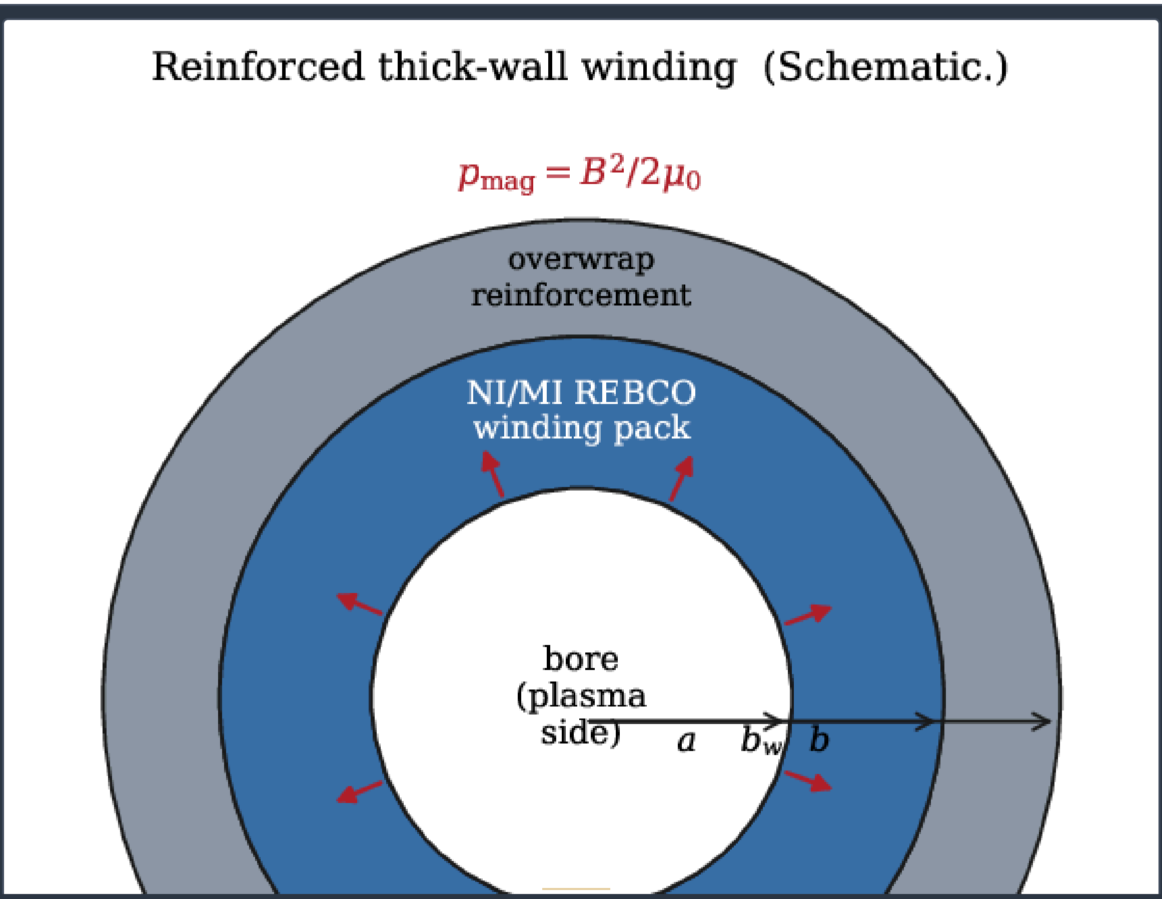
Reinforced thick-wall winding (Schematic.)
$p_{mag} = B^2/2\mu_0$
overwrap reinforcement
NI/MI REBCO winding pack
bore (plasma side)
a
b_w
b

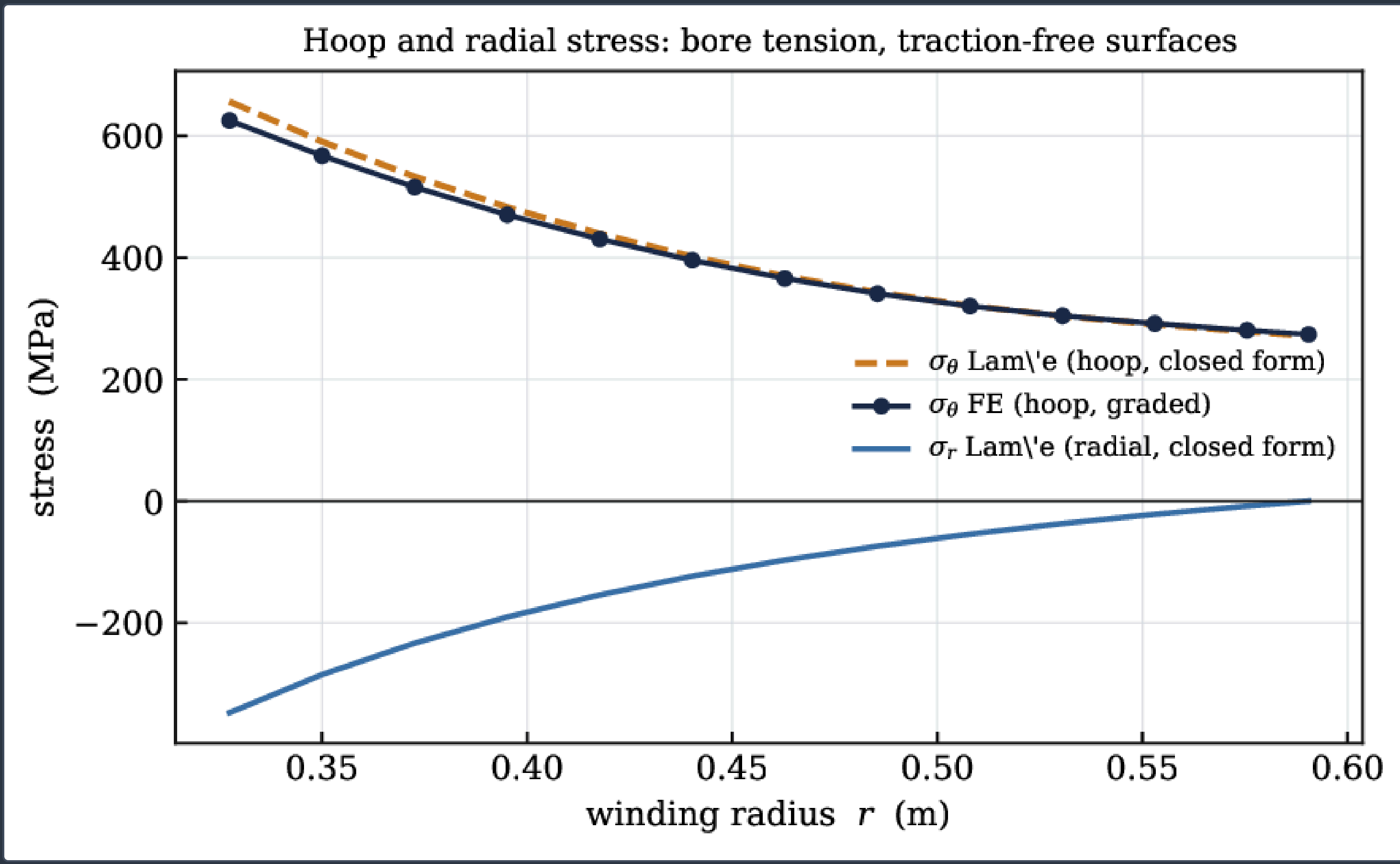

Hoop and radial stress across the winding. The finite-element hoop stress (data) tracks the closed-form Lam\'e hoop; the closed-form radial component is compressive, vanishing at both traction-free surfaces ($\sigma_r(a) = \sigma_r(b) = 0$) as the boundary-value problem of §2.3 requires.

MAGNETIC PRESSURE AND THE REINFORCEMENT BUDGET

The plug coil carries the heaviest bore load. Figure 9 plots the magnetic pressure of equation (5) against the reinforced allowable: $115/279/358\,MPa$ at $17/26.49/30\,T$, all below the $667\,MPa$ allowable, so a reinforced monolith can hold the field at every point (the condition $p_{\mathrm{mag}} < \sigma_{\mathrm{allow}}$ of equation 15 is met with room to spare). The corresponding required reinforcement thickness from equation (15) is plotted in figure 9: $0.16/0.48/0.71\,m$, sub-metre across the field range and within demonstrated overwrap practice. The quadratic growth of p_{mag} with field is visible directly as the steep rise of t_{req} from $17\,T$ to $30\,T$.

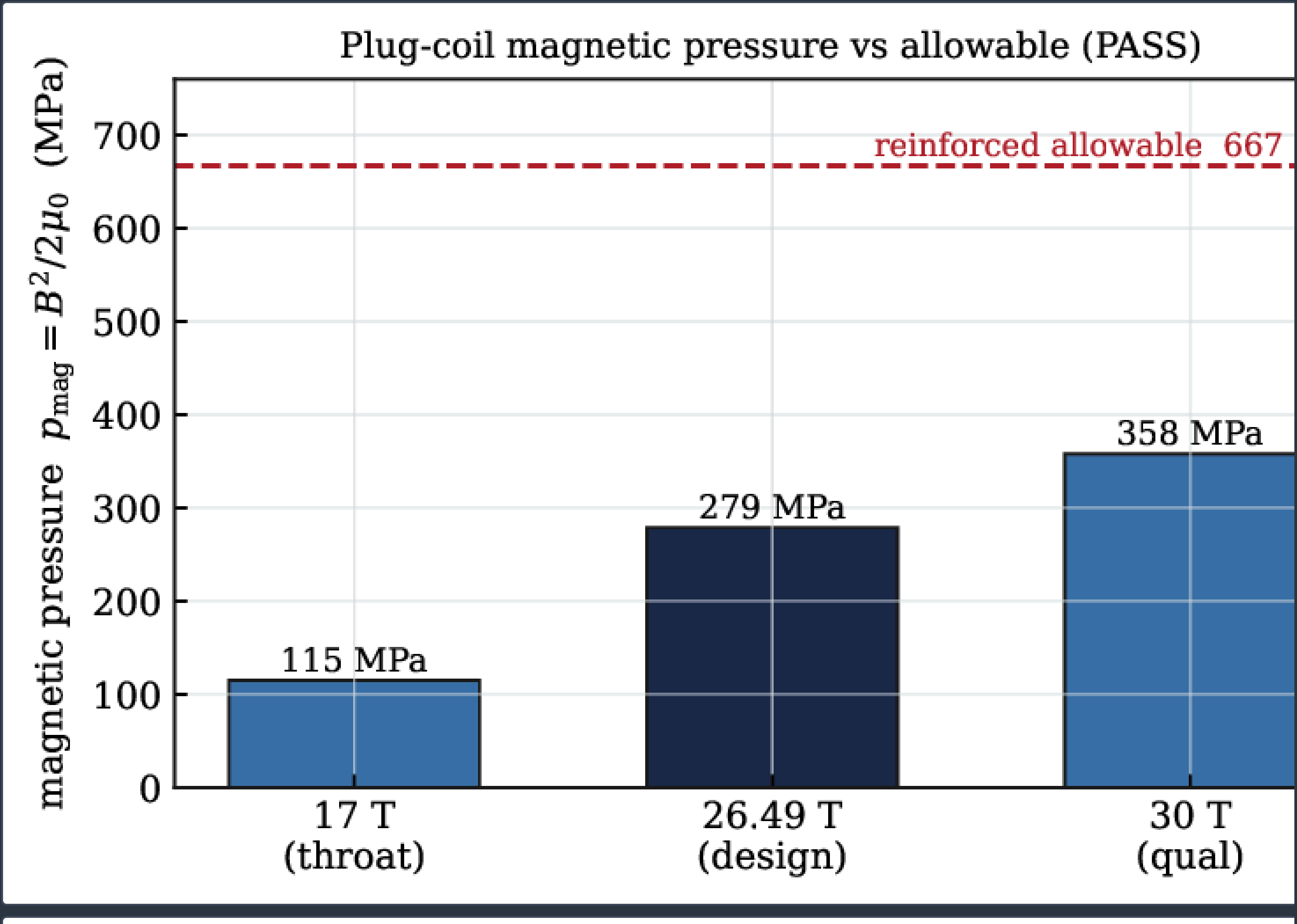
Plug-coil magnetic pressure vs allowable (PASS)
magnetic pressure $p_{mag} = B^2/2\mu_0$ (MPa)
reinforced allowable 667
115 MPa
279 MPa
358 MPa
17 T (throat)
26.49 T (design)
30 T (qual)
0
100
200
300
400
500
600
700

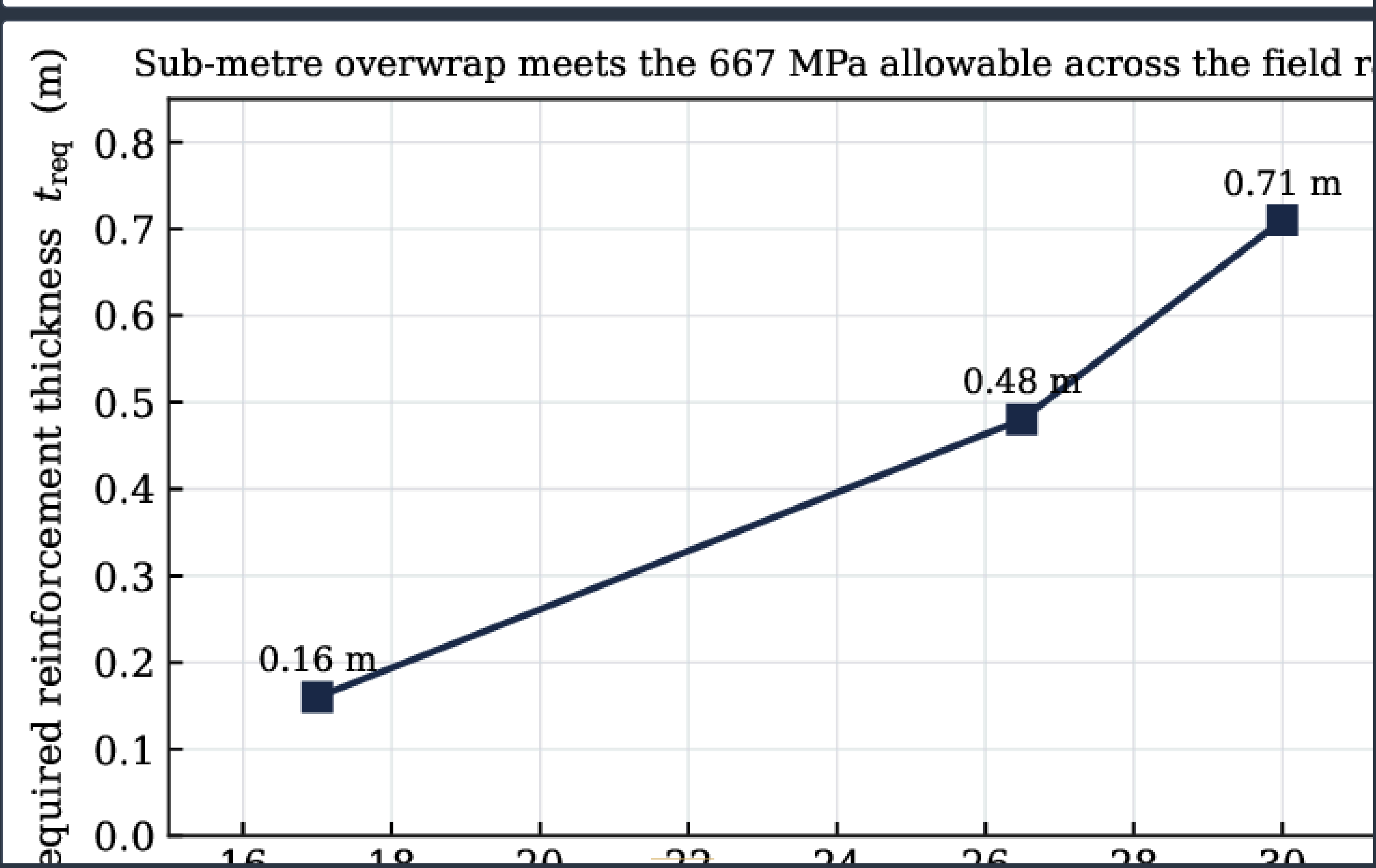
Sub-metre overwrap meets the 667 MPa allowable across the field r
equired reinforcement thickness t_{req} (m)
0.16 m
0.48 m
0.71 m
0.0
0.1
0.2
0.3
0.4
0.5
0.6
0.7
0.8

The conductor's own hoop stress, not the coil shell, is the tightest structural quantity. A conservative thin-wall screen places the $26.49\,T$ plug conductor hoop stress at $\sim 814\,MPa$, a margin factor of 0.86 against a $\sim 700\,MPa$ reinforced allowable — feasible but reinforcement-limited, and explicitly flagged for finite-element closure. The three-dimensional CAD FEA closes that margin to $1.34\times$ with the plug dimensions unchanged, and returns a 2.85–$3.54\times$ REBCO strain margin once the graded pre-load is applied (register P3-FEA-10; companion [49]). The thin-wall estimate was doing its job as a conservative screen; the real-CAD geometry and pre-load distribute the load.

THE STRAIN-FIRST ENVELOPE AND GRADED PER-TURN PRE-LOAD

The genuinely new engineering element is the graded per-turn pre-load derived in §2.6, which flattens the Lorentz strain gradient of equation (13). Figure 10 shows the mechanism directly: the bore-peaked Lorentz strain, the applied compressive pre-strain of equation (17), and the flat net strain that results. Figure 11 plots the peak REBCO hoop strain against field for three cases, scaled from the frozen finite-element anchors through the $p_{mag} \propto B^2$ law. Without pre-load the peak strain reaches 0.595% at $26.49\,T$ — above the 0.40% irreversible limit. The graded pre-load cuts the peak by 52.4% to 0.283% and flattens the profile roughly fourfold (register SC-BR-4). With thermal contraction and vertical load superposed, the peak rises to 0.365% at the design field — still under the limit — and closes to the limit only at the $30\,T$ qualification bound (register HX-09). On the as-drawn CAD the same graded pre-load returns a peak hoop strain of 0.151% on the centrepost ($2.65\times$ margin, jacket von Mises $579\,MPa$, $1.38\times$) and 2.85–$3.54\times$ margin on the plug (register P3-FEA-01, P3-FEA-10; the plug's three-dimensional structural FEA is developed in a companion paper [49]). The strain-first criterion of equation (19) is therefore met with margin at both magnets, with the pre-load method — not a new conductor material — doing the work.

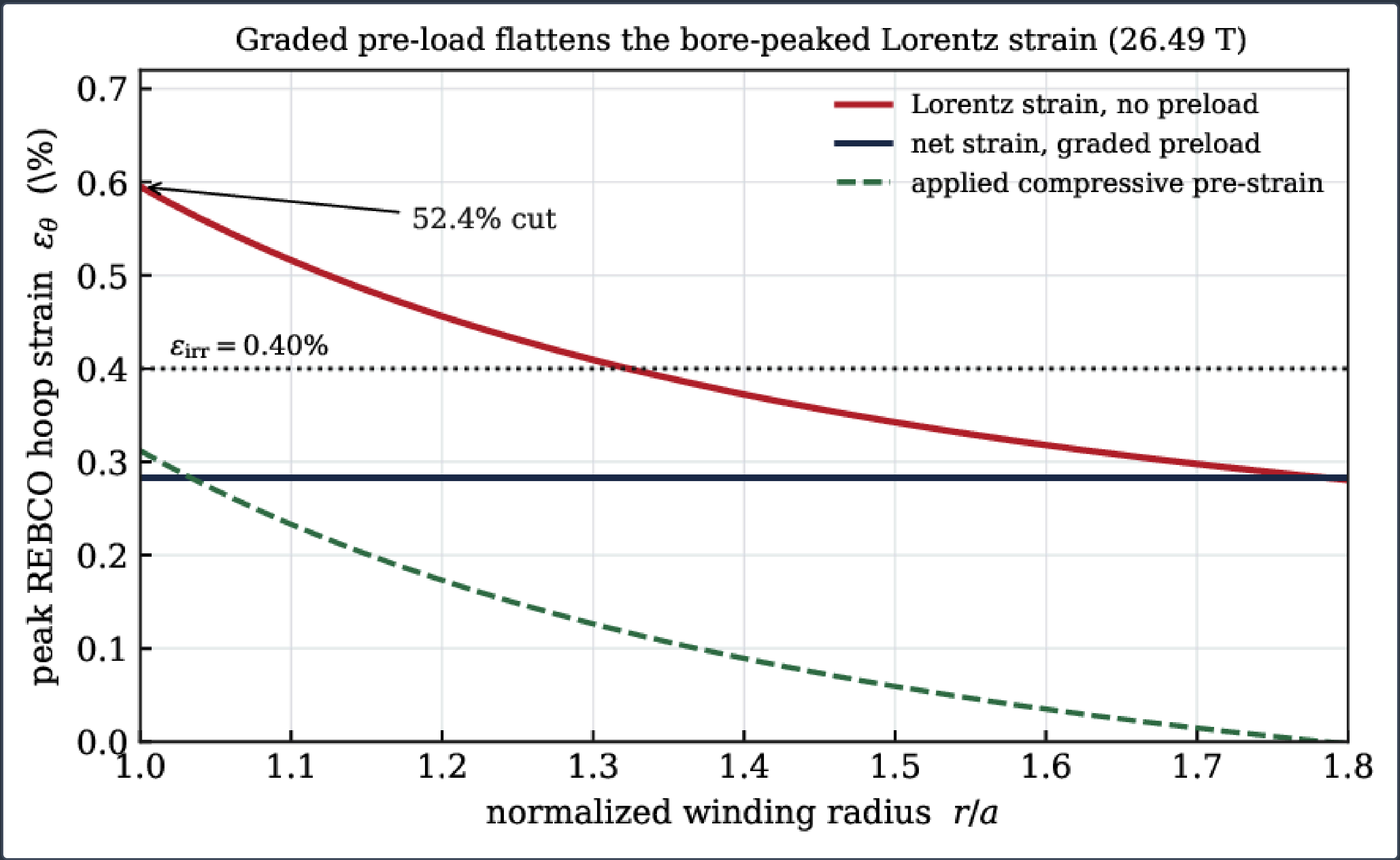

Graded per-turn pre-load. The bore-peaked Lorentz strain (red) is offset by an applied compressive pre-strain (green, equation 17) largest at the bore, giving a flat net operating strain (navy) held below ε_{irr}. At $26.49\,T$ the peak falls 52.4%, from 0.595% to 0.283% (register SC-BR-4/HX-09).

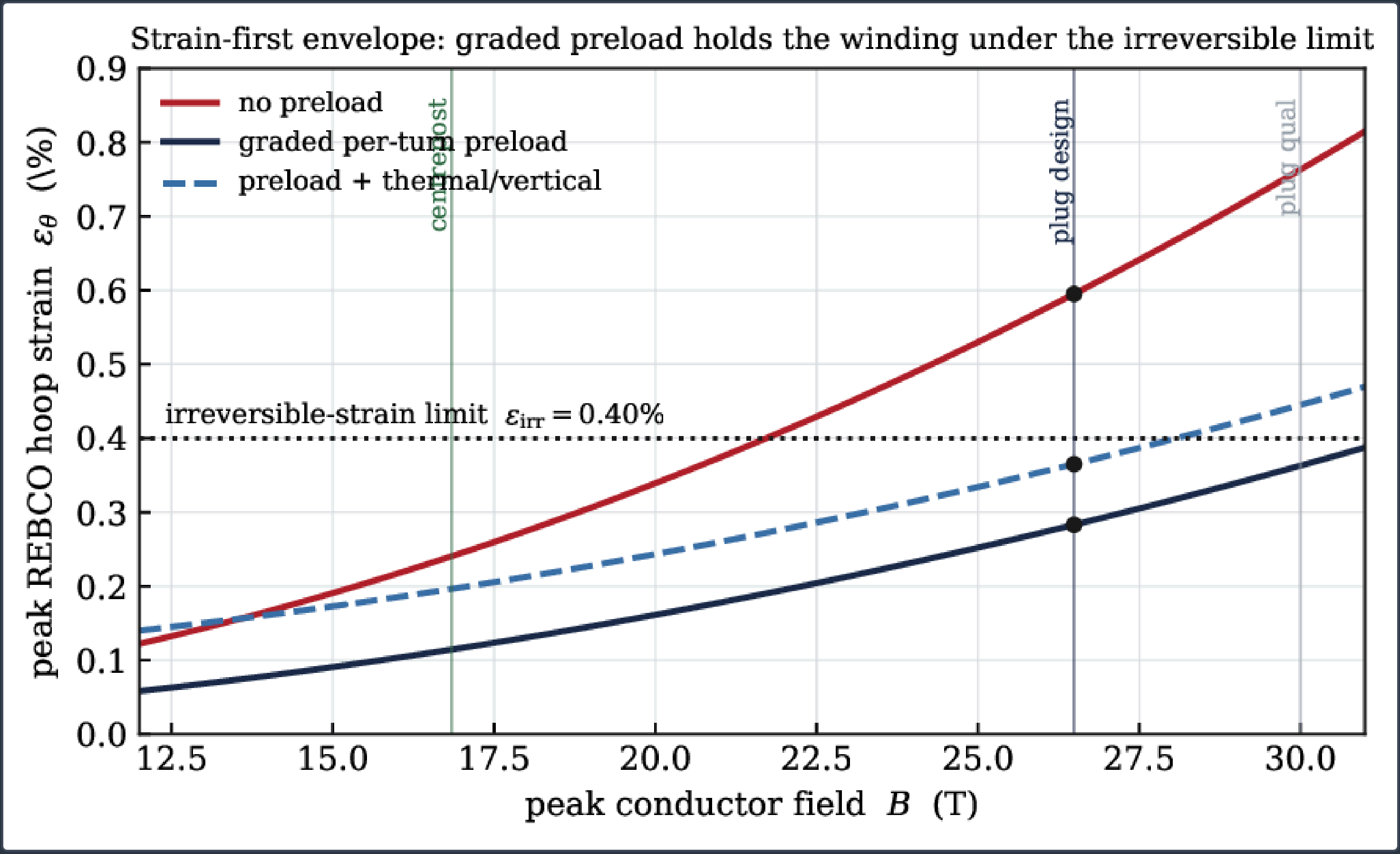

Strain-first envelope: peak REBCO hoop strain versus field for no pre-load, graded per-turn pre-load, and pre-load with thermal/vertical loads superposed, against the 0.40% irreversible limit. Curves are derived from the frozen finite-element anchors (register SC-BR-4, HX-09; markers) through the $p_{mag} \propto B^2$ Lorentz scaling, with the thermal/vertical contribution modelled as a field-independent offset.

THE TEMPERATURE-MARGIN LOAD LINE OF THE TWO MAGNETS

Figure 12 places the two distinct magnets on the load-fraction/temperature-margin plane of equations (20)–(21), and figure 12 shows the underlying critical-surface curves $I_c(T)/I_c(T_{op})$ on which each margin is read off. The breeder centrepost, at $16.84\,T$, runs at a load fraction $I_{op}/I_c \approx 0.27$ with a current-sharing margin $\Delta T \approx 49.5\,K$; the burner plug, at the higher $26.49\,T$, runs harder at load fraction ≈ 0.43 with $\Delta T \approx 37.1\,K$ (register KX-L1-A15). Both retain tens of kelvin of thermal headroom, a direct consequence of operating far below B_{c2} (figure 5). Crucially, the two points lie on *different* critical surfaces: the twin that models them — and the protection that guards them — treats the centrepost field and the plug field as the distinct quantities they are, never conflating $16.84\,T$ with $26.49\,T$.

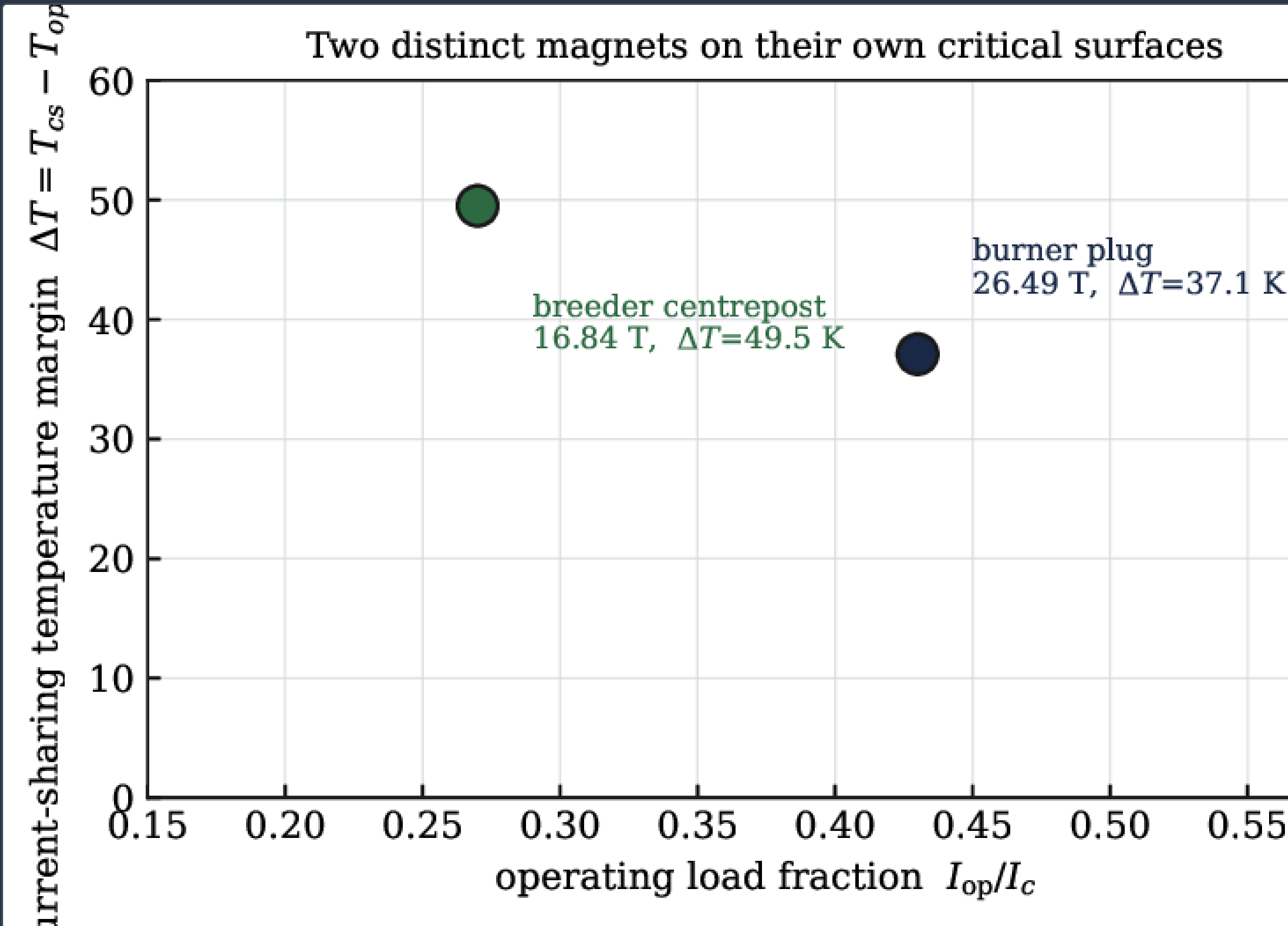
Two distinct magnets on their own critical surfaces
current-sharing temperature margin ΔT = T_cs − T_op
burner plug
26.49 T, ΔT=37.1 K
breeder centrepost
16.84 T, ΔT=49.5 K
operating load fraction I_op/I_c

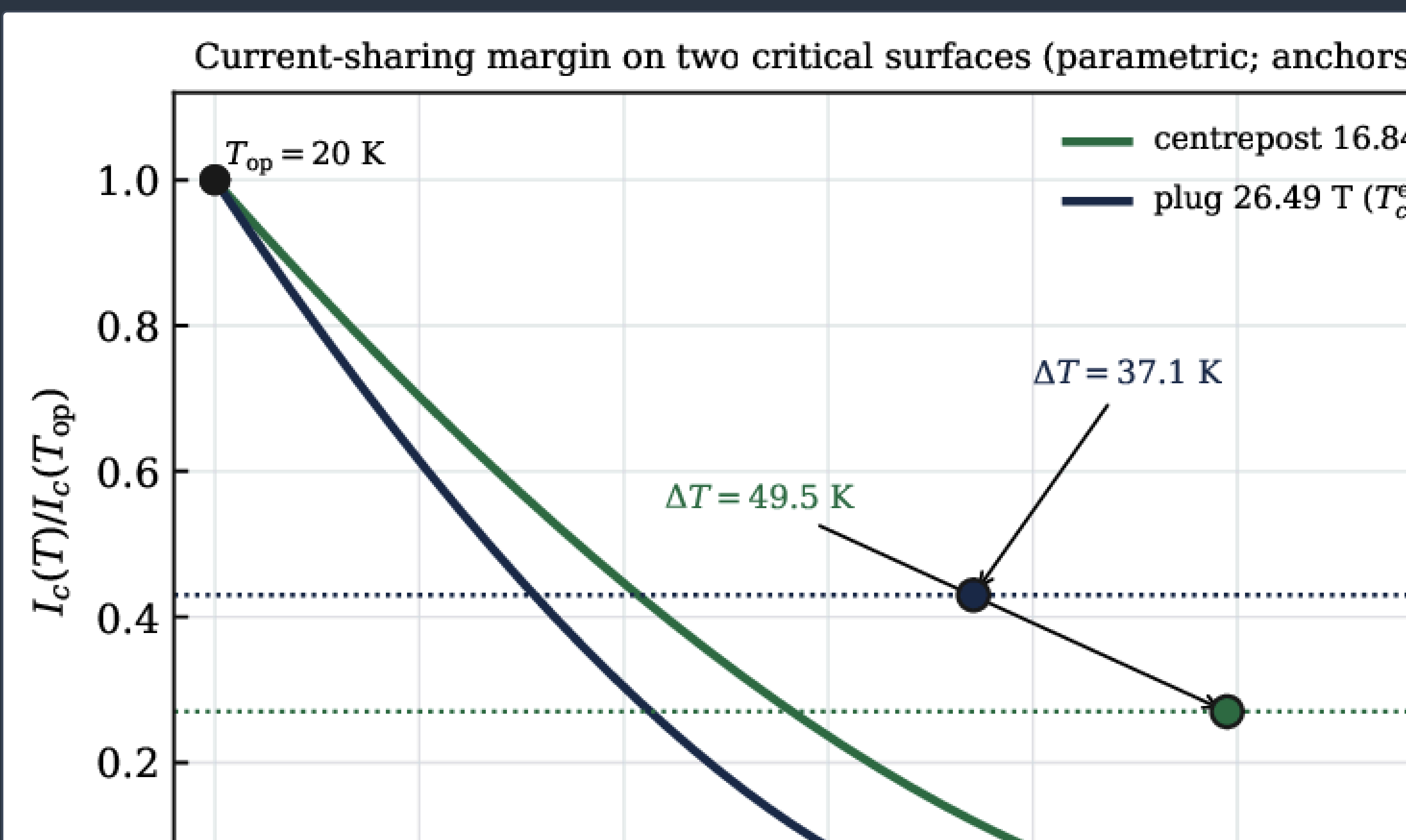
Current-sharing margin on two critical surfaces (parametric; anchors
T_op = 20 K
centrepost 16.84
plug 26.49 T
ΔT = 37.1 K
ΔT = 49.5 K
I_c(T)/I_c(T_op)

NEUTRON LIFETIME OF THE BREEDER CENTREPOST

Figure 13 shows the consumable-centrepost life law of equation (28). At the centrepost damage rate of 18.85 dpa fpy^{-1}, the fast-fluence rate — and hence the cartridge life — is a steep function of the inboard tungsten-carbide shield: a bare centrepost survives only 0.003 fpy, a 30 *cm* shield extends it to 0.221 fpy, and full (45 *cm*) shielding reaches 0.58 fpy, with the fast fluence falling two orders of magnitude from 2.9×10^{25} to 1.7×10^{23} $/m^2$ per full-power-year (register BR-L1-A13b). The centrepost is therefore designed as a scheduled-replacement cartridge, breeding from the outboard side while the inboard winding is consumed; the trade of coverage against protection, and the swap logistics, are the subject of companion papers [44,45], and the prognostic scheduling of the replacement cadence is developed separately [51].

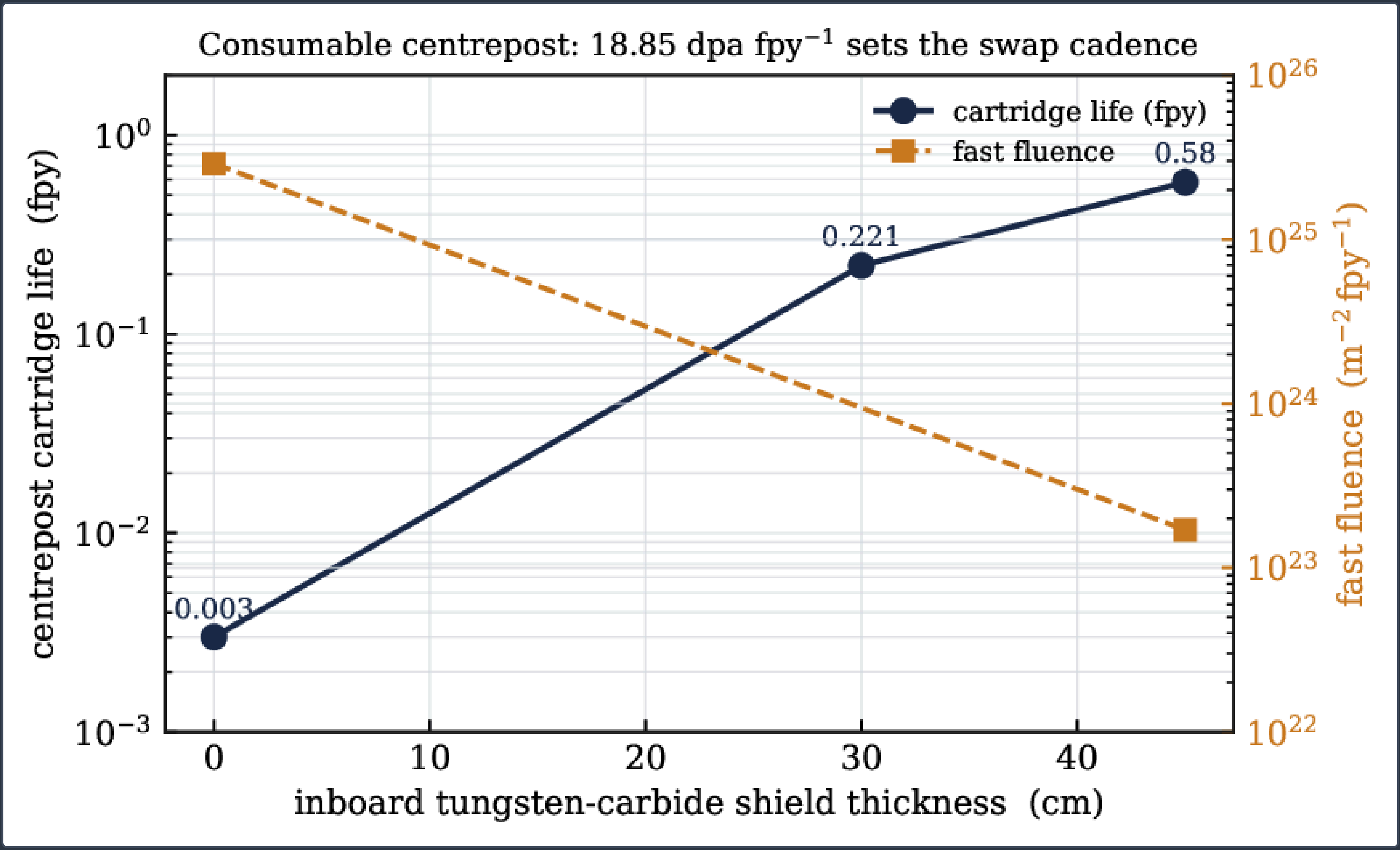

Consumable-centrepost life versus inboard tungsten-carbide shield thickness (left axis) and the corresponding fast-fluence rate (right axis). Anchored at register points BR-L1-A13b (0, 45 *cm*) and SC-BR-2 (30 *cm*); the connecting curve is a monotone interpolation of the anchors.

IRRADIATION TOLERANCE AND THE UN-DOPED-TAPE RULE

The break-even fluence Φ_{be} that enters equation (28) is itself a conductor-design result. Figure 14 compares the break-even fast fluence of an un-doped REBCO tape, 5.64×10^{22} , with that of a tape carrying engineered artificial pinning centres, 3.82×10^{22} (register BR-L2-A36, HX-22). The un-doped tape survives $1.48\times$ more fluence: the pinning defects that raise in-field I_c are the same sites that seed irreversible radiation damage, so for a lifetime-limited magnet the un-doped conductor is preferred — the "un-doped-tape rule" [46]. This is consistent with the systematic irradiation studies that find artificial-pinning-centre tapes degrade at lower fluence than plain tapes [16,15]. Both anchors exceed the 3.9×10^{22} $/m^2$ design rule the register upholds, and the first-principles basis of the degradation (chain-oxygen-vacancy formation) is developed in a companion paper [47].

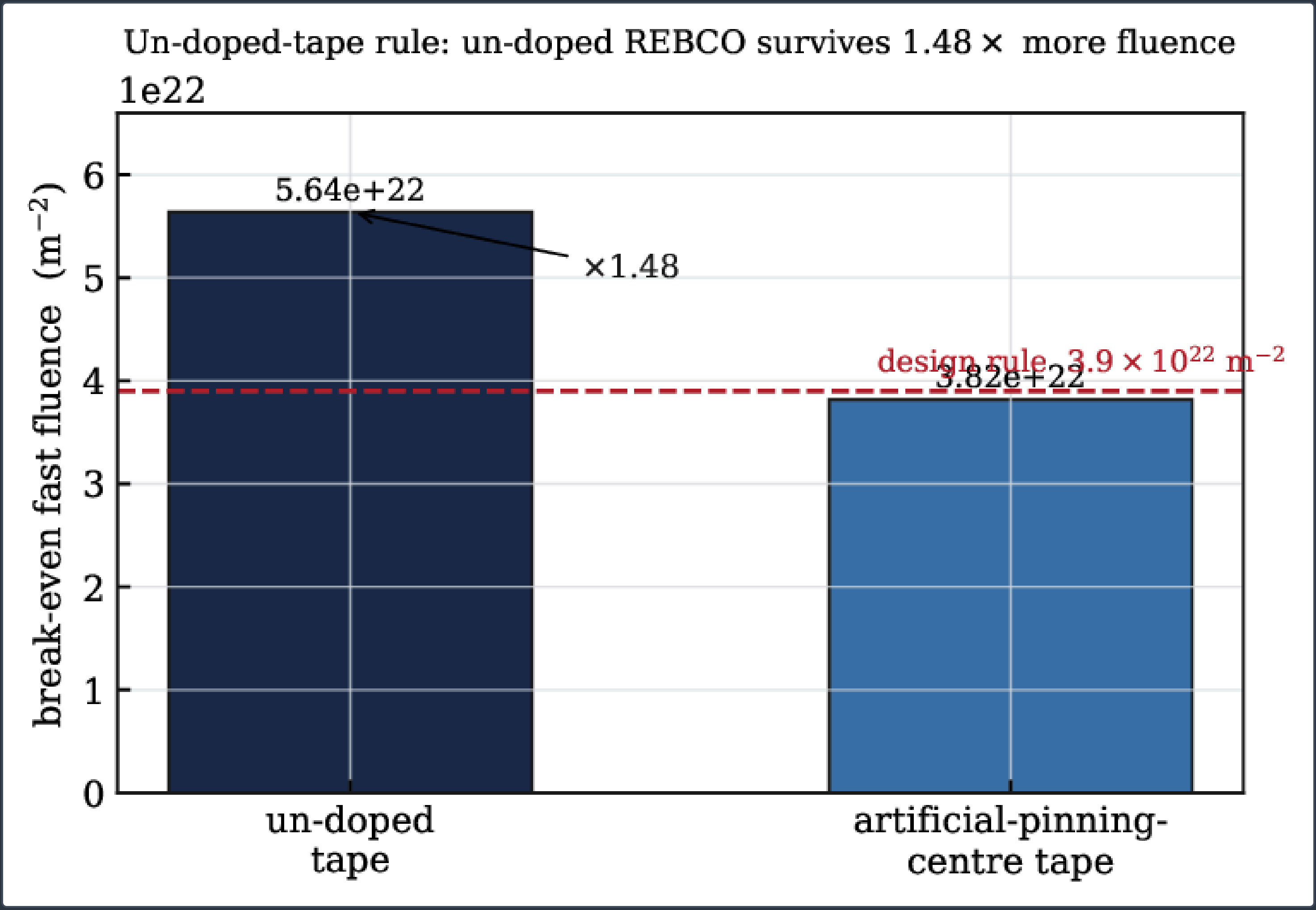

Break-even fast fluence of un-doped versus artificial-pinning-centre REBCO tape (register BR-L2-A36 / HX-22). The un-doped tape tolerates $1.48\times$ more fluence; both clear the 3.9×10^{22} $/m^2$ design rule.

THE COLD-MASS THERMAL BUDGET

Figure 15 makes the conductor-choice argument of §2.13 quantitative. A fully-resistive centrepost would dissipate $\approx 282\,MW$, $3.3\times$ the fusion power and a non-starter; the hybrid retains only a $\approx 39\,MW$ resistive sacrificial layer; and the fully-superconducting REBCO post reduces the burden to an $\approx 5\,MW$ cryogenic load, $\approx 56\times$ below the resistive case (register BR-CX-22). The Kronos baseline is a conduction-cooled dry winding, which removes the helium-expulsion hazard of a channel-cooled design entirely; the detailed cold-mass budget, current-lead loads and refrigeration plant are the subject of a companion paper [50].

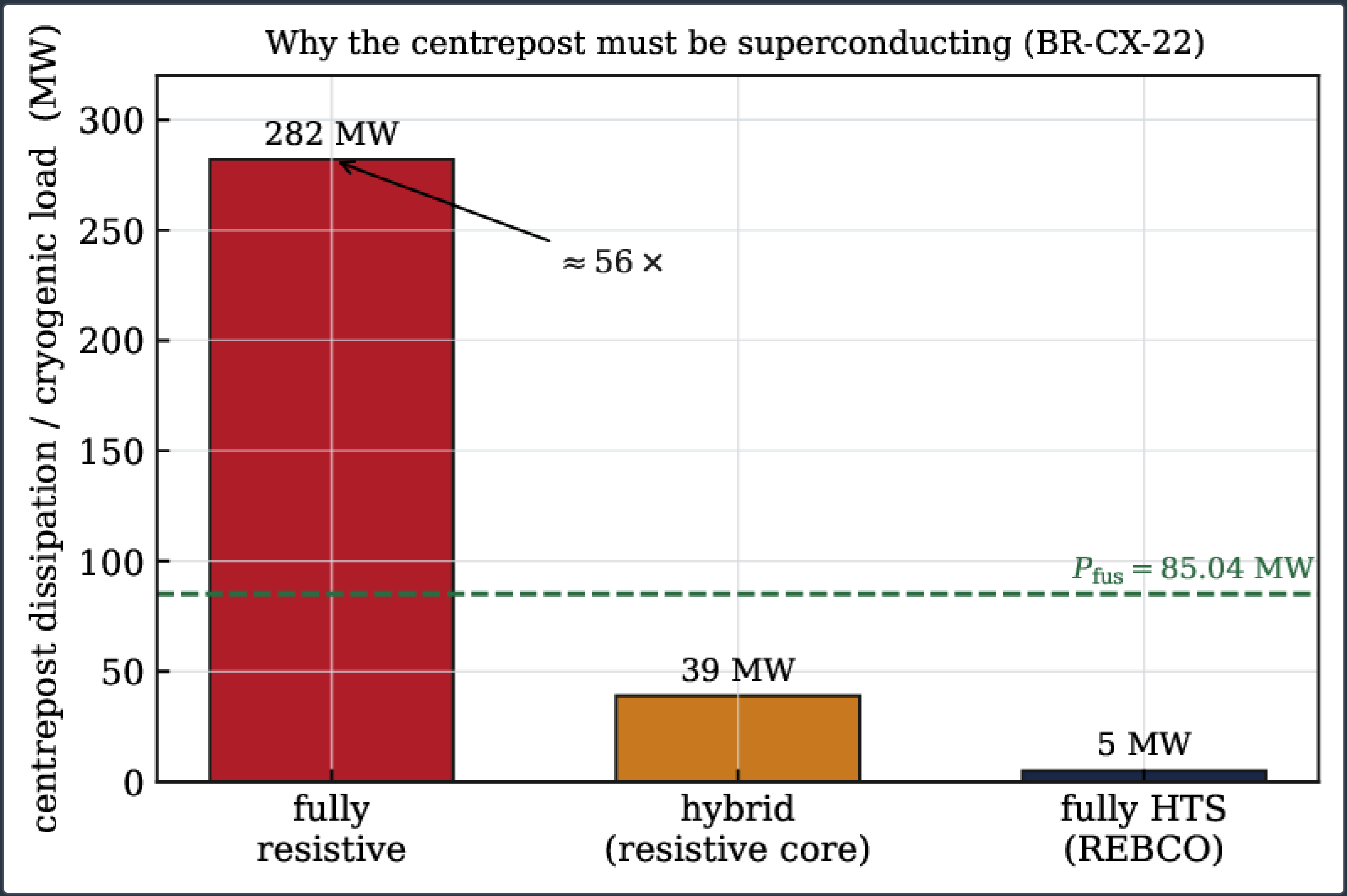

Centrepost cold-mass budget by conductor choice (register BR-CX-22), against $P_{\mathrm{fus}} = 85.04\,MW$. The fully-superconducting REBCO post reduces the dissipation $\approx 56\times$ below the resistive case, which is why the superconductor is not optional.

THE CONDUCTOR-QUANTITY BUDGET

The plug winding is a large object in conductor terms. At the plug the ampere-turn density is $13.5\,MA/m$, which at a $200\,A$ operating current is $\approx 6.8 \times 10^4$ turns per metre of coil, and of order $4 \times 10^2\ km$ of REBCO tape per metre of plug length at a $1\,m$ winding radius (register SC-BU-1). Figure 16 plots the tape length per metre of plug against winding radius; the linear growth is simply the circumference times the (radius-independent) turns-per-metre. These are demanding but not unreasonable quantities set against the $\sim 270\,km$ of tape wound into the SPARC toroidal-field model coil [13]; the fleet-scale tape-supply implications are treated in a companion paper [52].

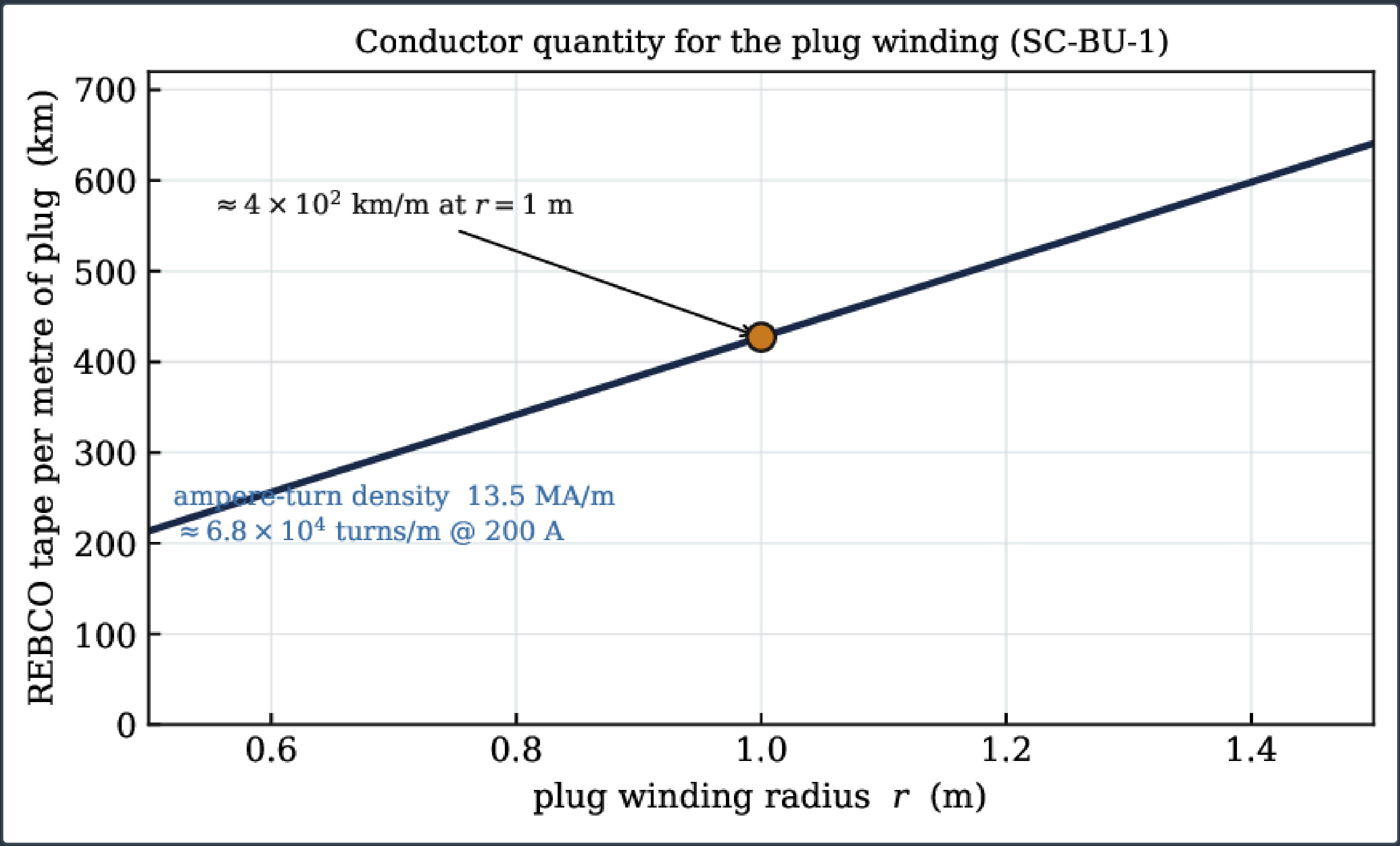

REBCO tape length per metre of plug winding versus winding radius (register SC-BU-1): $\approx 4 \times 10^2$ km at a $1\,m$ radius, from an ampere-turn density of $13.5\,MA/m$ and $\approx 6.8 \times 10^4$ turns per metre at $200\,A$.

WINDING PACK, JOINTS AND MANUFACTURING CONSIDERATIONS

The conductor-quantity budget of §4.10 has manufacturing consequences that the mechanics assume implicitly. Three are worth stating. First, kilometre-scale tape cannot be wound joint-free, so the winding carries lap or bridge joints whose resistance adds a distributed heat load and whose local stiffness perturbs the pre-strain profile of §2.6; the graded pre-load is specified per-turn precisely so that a joint can be accommodated by a local adjustment without breaking the flat net-strain condition of equation (16). Second, the reinforced thick-wall geometry of figure 7 is realised as co-wound or overwrapped structural tape, not as a separate external cylinder, so the homogenised moduli of §2.4 apply turn-by-turn and the reinforcement is placed where the Lam\'e hoop stress is largest — at the bore — rather than uniformly. Third, the no-insulation architecture removes the turn-to-turn insulation that would otherwise dominate the winding-pack thickness and the turn-to-turn thermal resistance, which is what makes the sub-metre reinforcement of figure 9 geometrically compatible with the ampere-turn density of §4.10. None of these is a solved manufacturing problem; they are the constraints a build campaign inherits, and they are recorded as such in the register. The fleet-scale tape-supply and fabrication bottlenecks are analysed separately [52].

QUENCH PROTECTION BUDGET AND FUSED PRECURSOR DETECTION

The seconds-scale MIITs budget of equation (25) is plotted in figure 17: the allowable detect-and-dump time falls from $4\,s$ at a $100\,A/mm^2$ stabiliser density to $1.9\,s$ at $200\,A/mm^2$, keeping the hot spot below $150\,K$ (register HX-10). That budget is protected by early precursor detection. Because NI REBCO has a slow v_{NZP}, a developing hot spot can reach a damaging temperature before it produces a measurable resistive voltage, so the twin fuses two non-voltage channels: a fibre-Bragg strain-rate channel reading the mechanical signature of local current redistribution, and a magnetization channel reading the collapse of the screening current. Their quadrature fusion dominates either channel across the receiver-operating characteristic (figure 18, table 3; register KX-L1-A20): area under the curve 0.992 against 0.976 (magnetization) and 0.921 (strain), and — most importantly at the 1% false-positive rate a protection trip demands — a true-positive rate of 0.857 against 0.671 and 0.372. The fusion gain is largest in exactly the low-false-alarm corner where a trip is decided. Figure 17 shows the timing consequence: the fused detector fires at $0.089\,s$, some $2.935\,s$ ahead of the $3.024\,s$ voltage threshold, at a signal-to-noise ratio of 322.5. An in-winding NV-diamond magnetometer provides a local vector precursor at a shot-noise-limited $0.189\,picoT\,\mathrm{Hz}^{-1/2}$ over a 125 Hertz$bandwidth, withaper-shotsignal-to-noiseratiooforder10^9againstthe$\!100 mT$ field step of a shed NI turn (register KX-L1-A22); the detection is developed fully in the companion quench-sensing paper [48].

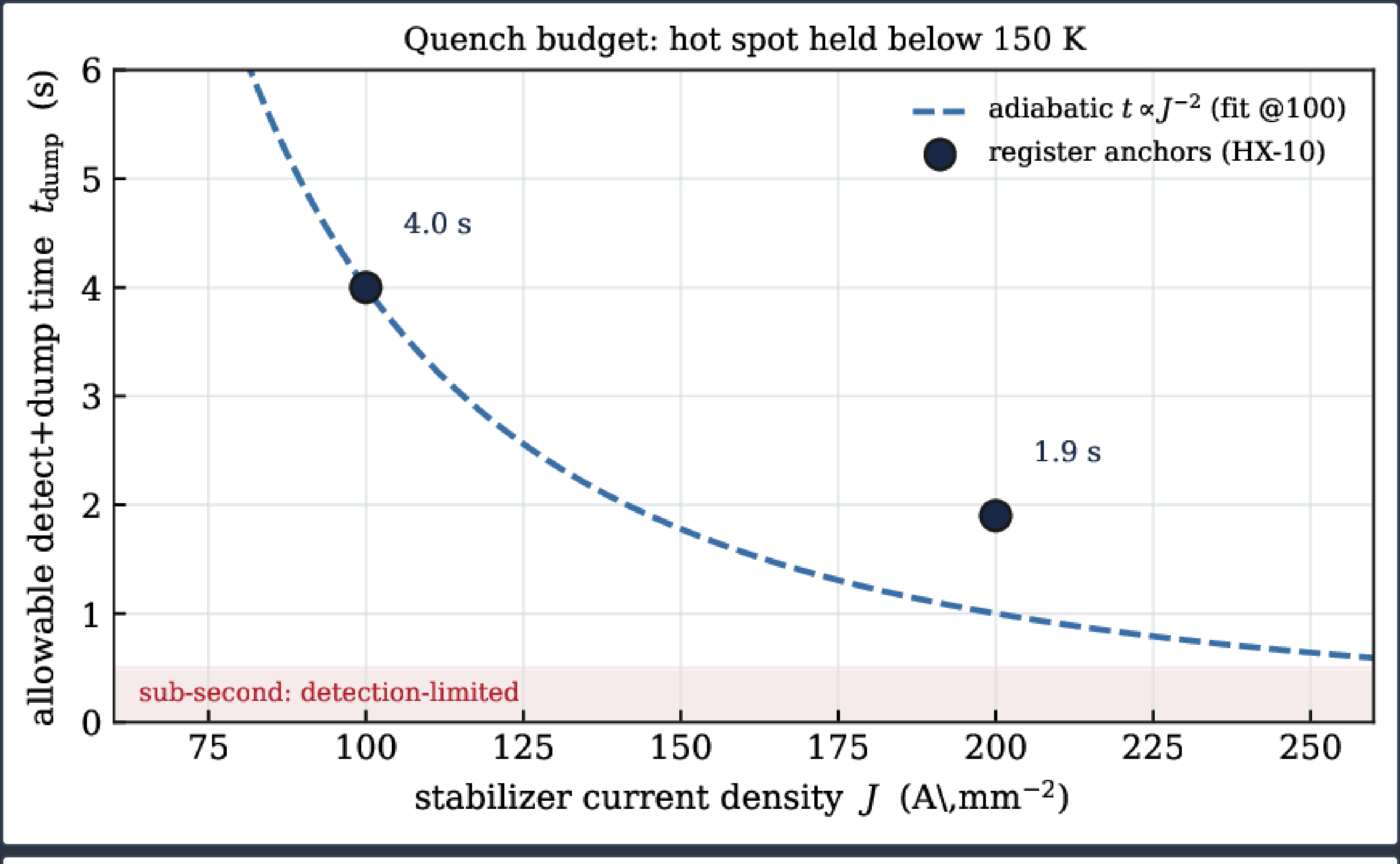

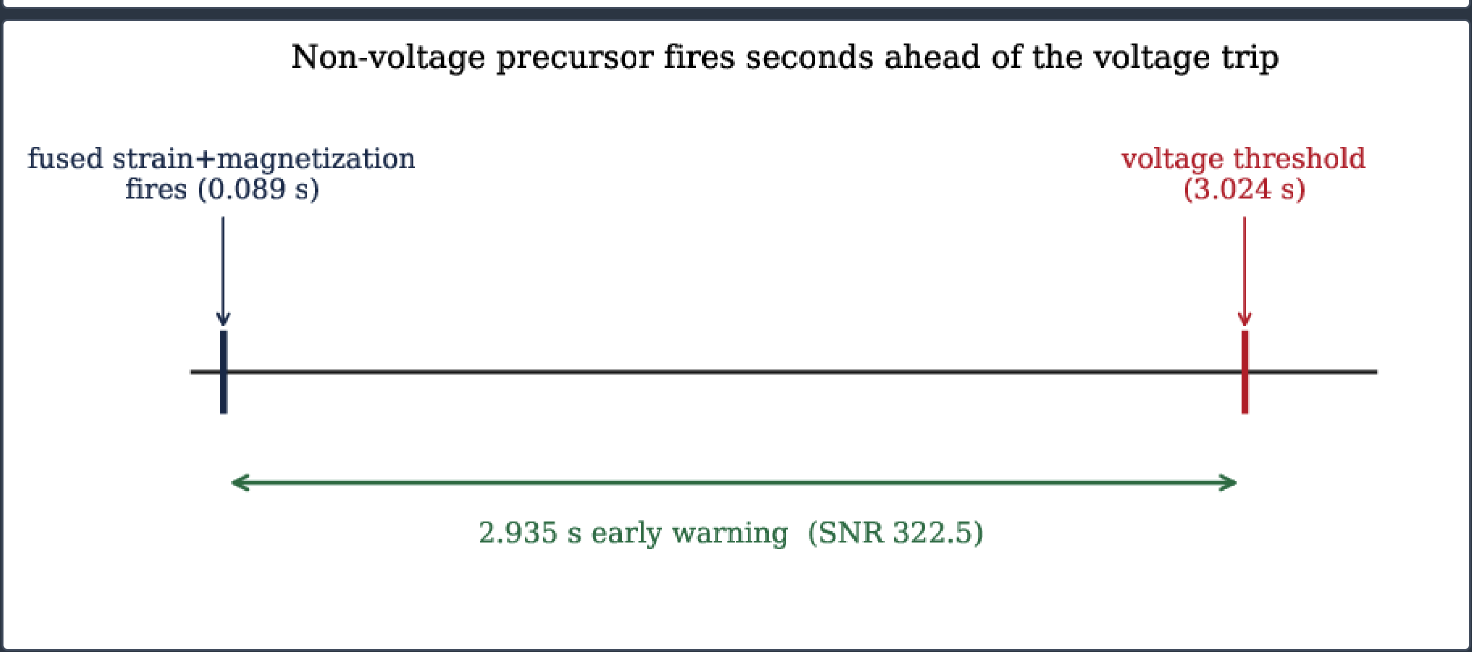

Adiabatic MIITs quench budget (register HX-10): allowable detect-and-dump time versus stabiliser current density, holding the hot spot below $150\,K$. Anchors at 100 and $200\ A/mm^2$; the dashed curve is the pure $t \propto J^{-2}$ adiabatic law fitted at 100.

CHANNEL	AUC	TPR @ 1% FPR	TPR @ 0.1% FPR
fibre-Bragg strain-rate	0.921	0.372	0.135
magnetization	0.976	0.671	0.386
fused (strain-rate + magnetization)	**0.992**	**0.857**	**0.597**

Fused quench-precursor detection (register KX-L1-A20; frozen synthetic, 2×10^4 trials/class). The fused detector dominates the full ROC and is strongest in the low-false-alarm corner.

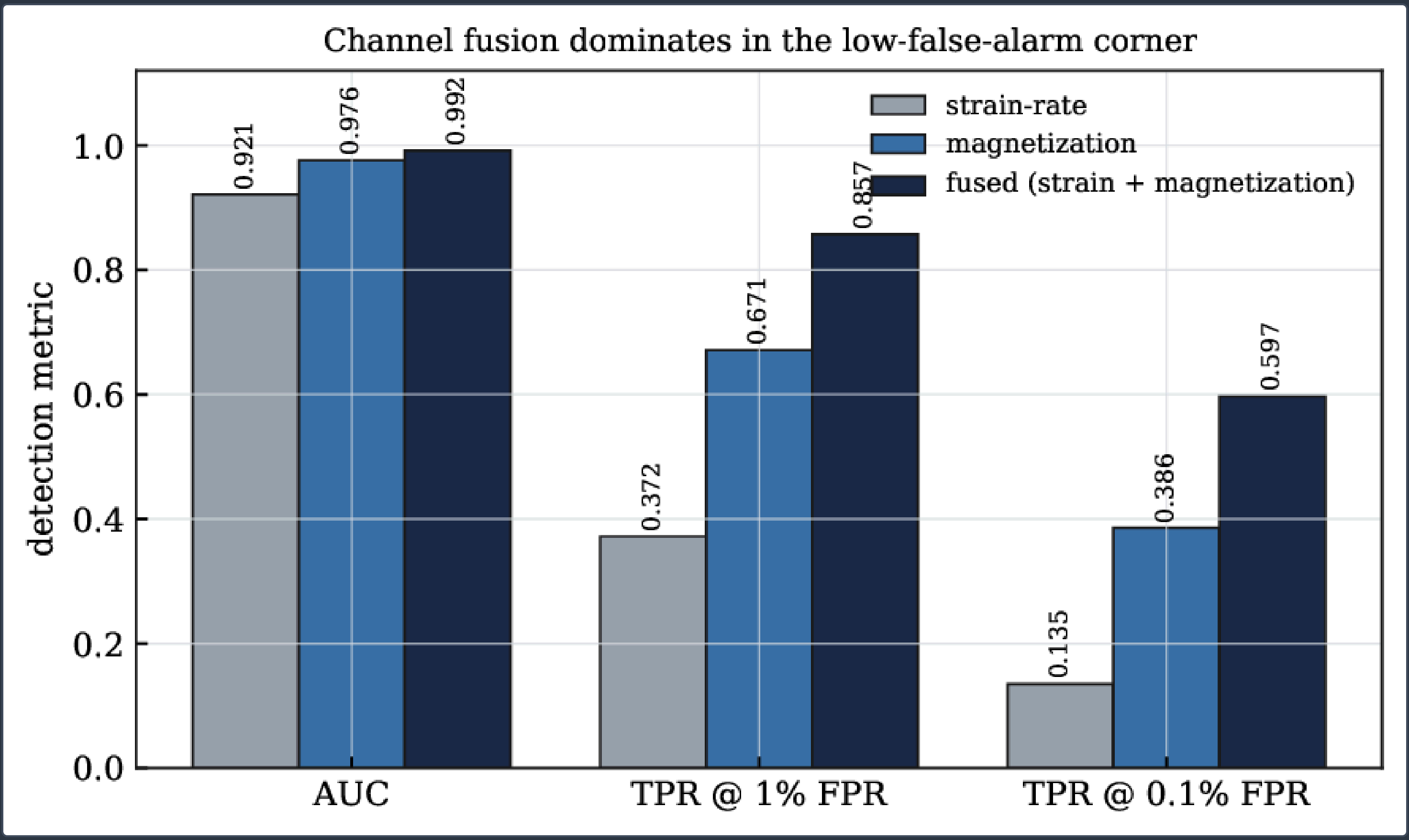

Fused quench-precursor detection metrics (register KX-L1-A20). The fused channel dominates either single channel, with its advantage growing as the false-positive tolerance tightens toward the trip-relevant corner.

INTERNAL CONSISTENCY OF THE FROZEN ANCHOR SET

Because every headline number is a frozen register anchor, the analysis admits internal consistency checks that a free-parameter model would not, and passing them is part of the evidence. Three are immediate. First, the magnetic pressure: $p_{\text{mag}} = B^2/2\mu_0$ at the plug design field $B = 26.49\,T$ evaluates to $(26.49)^2/(2 \times 4\pi \times 10^{-7}) = 279\,MPa$, reproducing the register anchor of equation (5) to the quoted precision, and the same expression at 17 and $30\,T$ returns 115 and $358\,MPa$. Second, the self-field: the peak-to-on-axis ratio $16.84/8 = 2.105$ equals $R_0/R_c = 1.20/0.57$, so the canonical centrepost peak, on-axis field and major radius are mutually consistent through Amp\`ere's law (§2.2). Third, the strain reduction: the graded pre-load anchor $0.595\% \to 0.283\%$ is a $1 - 0.283/0.595 = 52.4\%$ cut, matching the register figure, and the residual 0.365% with thermal and vertical loads is the 0.283% pre-loaded value plus a field-independent 0.082% offset, exactly as figure 11 models it. That the independently-frozen anchors close these identities — pressure from field, field ratio from geometry, strain cut from the two strain anchors — is a check on the register, not an assumption of it.

BOTH MAGNETS QUALIFY

Table 4 collects the result, and figure 19 presents the same qualification as a margin scorecard. Under one bore-resolved mechanics benchmarked against the closed form, both magnets qualify structurally, by different margins and against different binding limits. The centrepost is stress-comfortable and neutron-lifetime-limited; the plug is more heavily loaded but still meets its allowable at the required bore. The plug-coil *structural* gate is thereby retired by qualification, not asserted; the residual burner gate lies in the plug-potential physics analysed in the burner papers [41,42,43], not in the magnet.

QUANTITY	BREEDER CENTREPOST	BURNER PLUG
peak field	$16.84\,T$	$26.49\,T$ (design)
field / B_{c2}	0.17	0.26
magnetic pressure	—	$115/279/358\,MPa$ $(17/26.49/30\,T)$
reinforcement t_{req}	(stress-comfortable)	$0.16/0.48/0.71\,m$ vs $667\,MPa$
peak hoop strain (graded pre-load)	0.151% CAD	0.283% (0.365% w/ thermal+vertical)
load fraction I_{op}/I_c	0.27	0.43
temperature margin ΔT	$49.5\,K$	$37.1\,K$
binding limit	neutron life (0.58 fpy)	winding strain at required bore
structural verdict	PASS	PASS (FE ratio 0.66)

Both REBCO magnets qualify under one bore-resolved mechanics. Fields are canonical register values; all numbers are design targets or model outputs, not measurements.

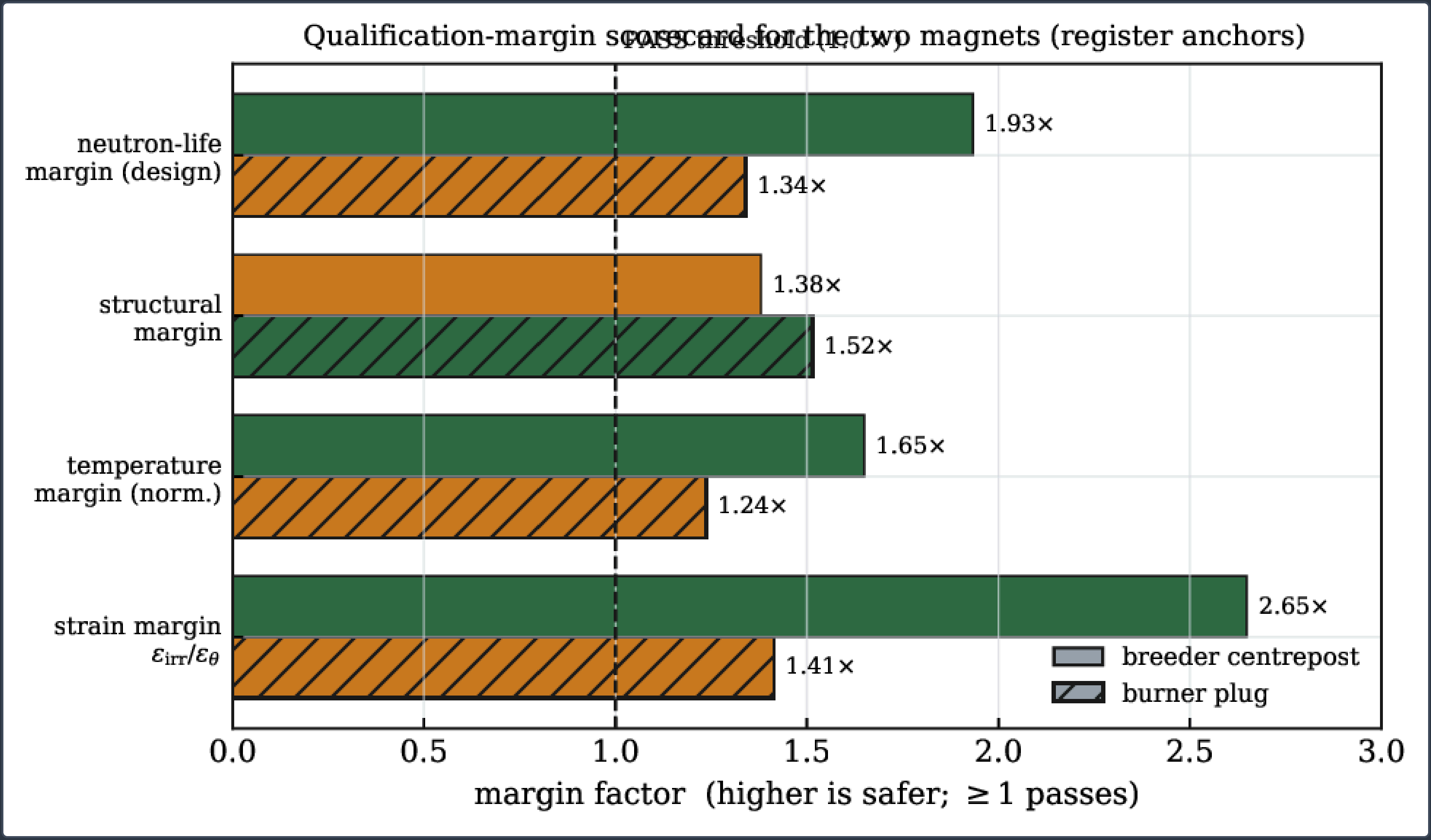

Qualification-margin scorecard (register anchors). For both magnets the strain, temperature, structural and neutron-life-design margins meet or exceed the 1.0× pass threshold; the centrepost is comfortable across the board and neutron-life-limited by design choice, the plug more heavily loaded but passing at its required bore.

§ 5

Magnet protection philosophy: no-insulation versus alternatives

The quench results of §4.12 are best understood as one point in a three-way trade among winding architectures, and it is worth setting the trade out explicitly because it is the single most consequential protection decision. An *insulated* winding charges fast and its field tracks the terminal current with no lag, but it has no self-protection: a hot spot that outruns the voltage detector (the slow-v_{NZP} problem of [30]) can burn out before the external dump acts, and the full magnetic energy must be extracted through the terminals. A *no-insulation* (NI) winding is the opposite: current sheds radially around a normal zone (figure 3), so the coil is intrinsically self-protecting and mechanically robust, at the cost of the charging lag and ramp loss of equation (24). A *metal-insulation* (MI) winding interpolates, raising the turn-to-turn resistance R_{ct} to recover ramp speed while retaining partial self-protection. Table 5 summarises the trade. The Kronos choice is NI/MI with a V_2O_3 smart interlayer whose resistance is temperature- switched, so the winding presents a high R_{ct} (fast, low-loss) at operating temperature and a low R_{ct} (self-protecting) exactly where a hot spot forms — capturing the ramp behaviour of MI and the self-protection of NI in one conductor. The fused precursor of §4.12 is layered on top: it does not replace self-protection but shortens the detection time so that the seconds-scale MIITs budget of figure 17 is never approached, and it is the one place where the NV magnetometer's open neutron-tolerance item (§9) enters.

ATTRIBUTE	INSULATED	NO-INSULATION (NI)	METAL-INSULATION (MI)
turn-to-turn resistance	∞	very low	intermediate
charging lag τ_{NI}	none	long	moderate
ramp ohmic loss	none	higher	lower
self-protection	none	intrinsic	partial
mechanical robustness	lower	high	high
Kronos use	—	2cNI/MI with V_2O_3 smart interlayer	

Winding-architecture trade. The Kronos NI/MI choice with a V_2O_3 temperature-switched interlayer aims to capture the ramp behaviour of MI and the self-protection of NI in a single conductor.

§ 6

Sensitivity and uncertainty quantification

A design-target study is only as useful as its robustness to the inputs it assumes, so we quantify how the two governing outputs — the peak REBCO hoop strain and the required reinforcement — respond to the parameters that carry the most uncertainty.

SENSITIVITY OF THE GOVERNING STRAIN

Because the peak strain follows $\varepsilon_\theta^{\max} \propto p_{\text{mag}}/E_\theta \propto B^2\,(b^2+a^2)/[(b^2-a^2)E_\theta]$ from equations (14)–(19), its parameter sensitivities are analytic. A $\pm5\%$ excursion in field moves the strain by $\pm10.25\%$ (the quadratic dependence), the single largest lever; a $\pm10\%$ excursion in the effective in-tape modulus E_θ moves it by $\mp9.1\%$; and the reinforcement thickness, allowable stress and Poisson ratio are progressively weaker. The additive thermal/vertical offset is the second-largest contributor at the design field. Figure 20 ranks these as a tornado diagram about the 0.283% pre-loaded base; the important conclusion is that even the worst-case stacking of adverse excursions keeps the design-field strain below the 0.40% irreversible limit, and that field control is the sensitivity that most rewards attention.

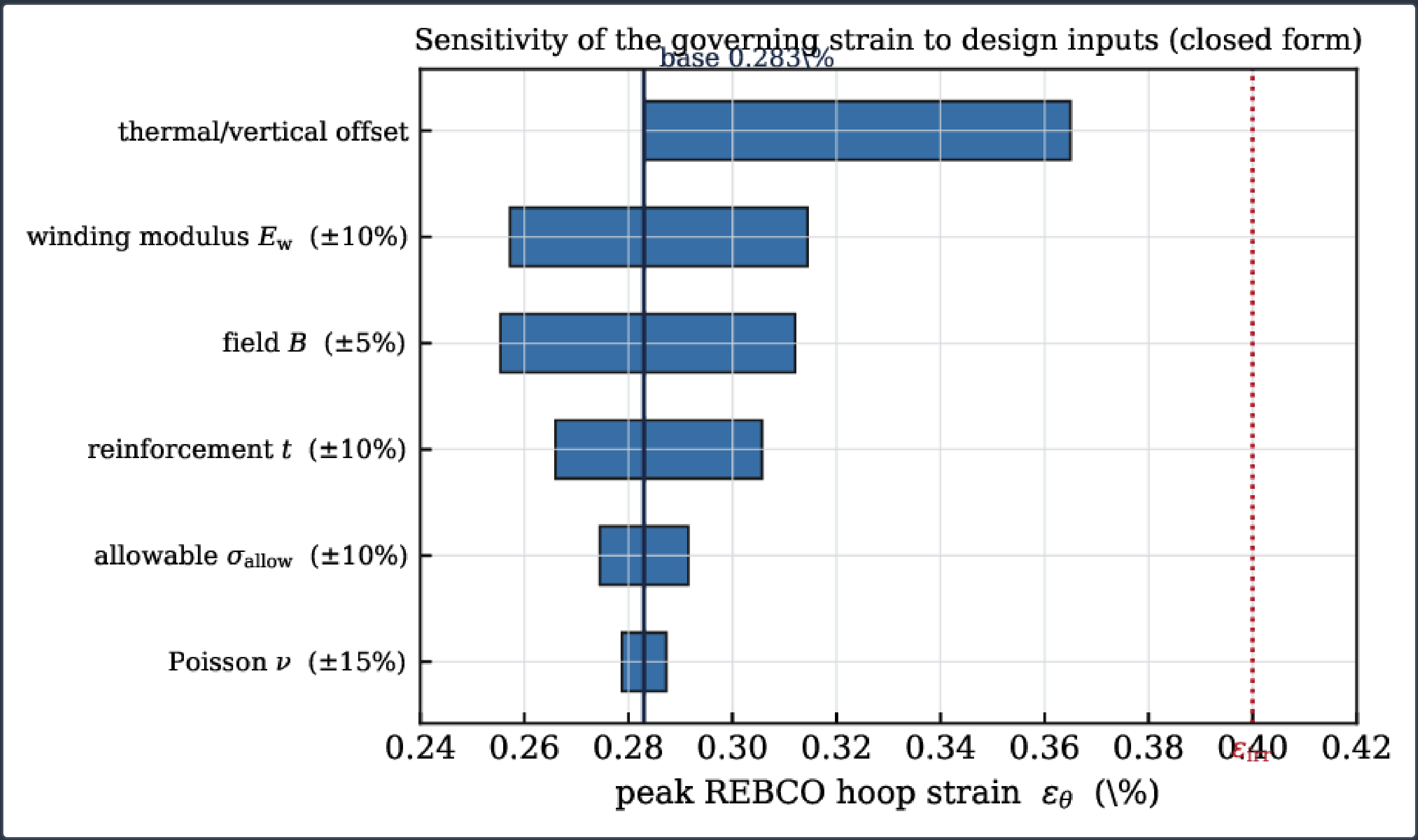

Tornado sensitivity of the peak REBCO hoop strain to design inputs about the 0.283% graded-pre-load base, computed from the closed-form scaling $\varepsilon_\theta^{\max} \propto B^2/E_\theta$. Field is the dominant lever; the worst-case stack stays below $\varepsilon_{\text{irr}} = 0.40\%$.

SENSITIVITY OF THE REINFORCEMENT BUDGET

The required reinforcement of equation (15) diverges as the allowable approaches the magnetic pressure, $\sigma_{\text{allow}} \to p_{\text{mag}}$, so the reinforcement is most sensitive to the structural allowable when the two are close. Figure 21 sweeps the allowable at the $26.49\,T$ design field ($p_{\text{mag}} = 279\,MPa$): at the baseline $667\,MPa$ the budget is $0.48\,m$ and the curve is flat, so a $\pm 10\%$ uncertainty in the allowable changes the wall by only a few centimetres; the budget becomes sensitive only if the allowable is degraded toward $\sim 350\,MPa$. This is the quantitative statement that the plug reinforcement sits in a comfortable, not a marginal, part of the design space.

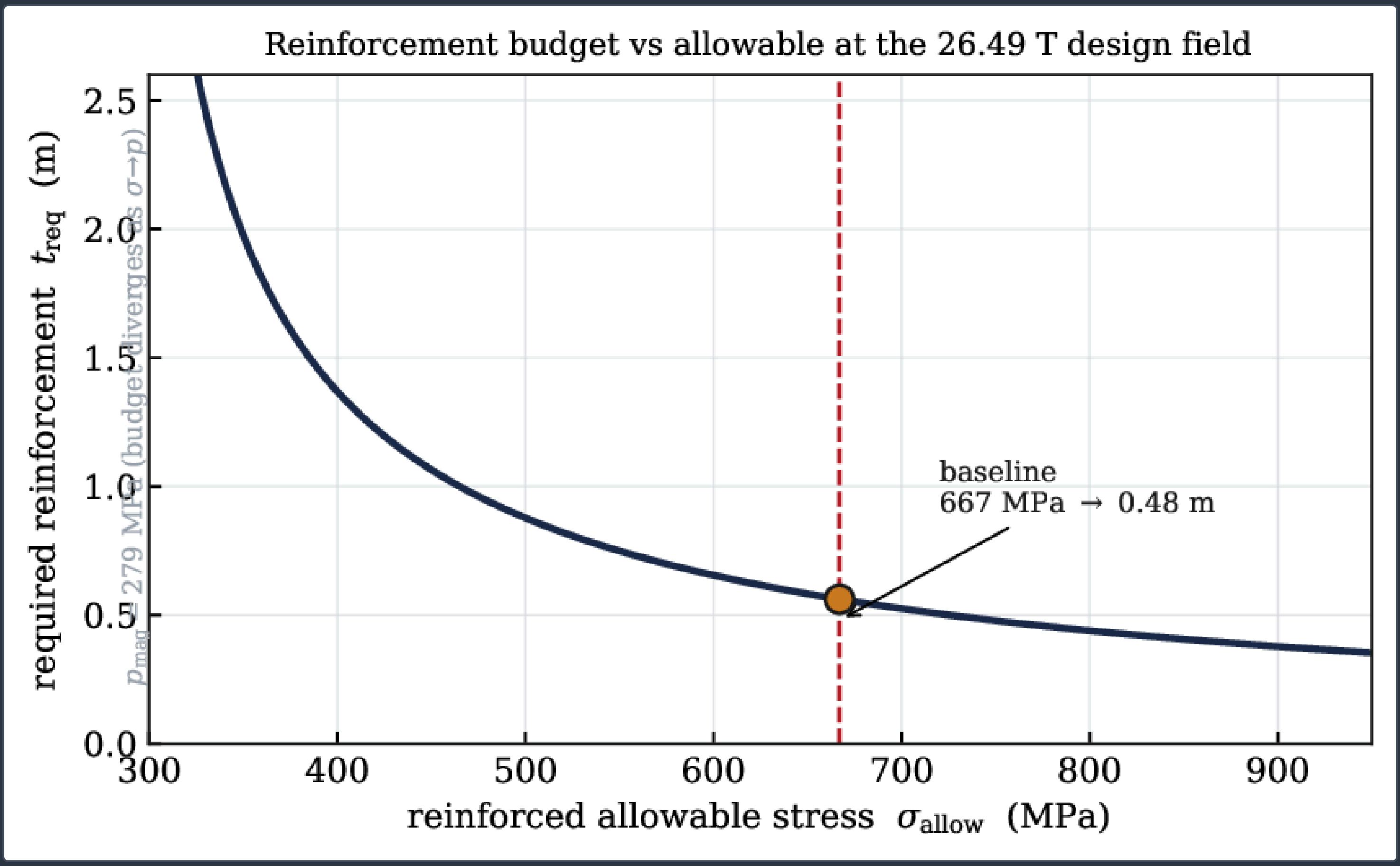

Required reinforcement versus reinforced allowable at the $26.49\,T$ design field ($p_{\text{mag}} = 279\,MPa$, equation 15). The baseline $667\,MPa$ sits on the flat part of the curve; the budget diverges only as $\sigma_{\text{allow}} \to p_{\text{mag}}$.

AGGREGATED UNCERTAINTY STATEMENT

Combining the sensitivities above, the plug at its design field carries a strain margin to ε_{irr} of $0.40/0.365 = 1.10$ with all adverse loads superposed and $0.40/0.283 = 1.41$ under the graded pre-load alone, a reinforcement margin insensitive to a $\pm 10\%$ allowable excursion, and a temperature margin of $37.1\,K$; the centrepost carries a strain margin of $2.65\times$ on the CAD, a temperature margin of $49.5\,K$, and a binding neutron-life margin that is a design choice (shield thickness) rather than a physical ceiling. The one item that is genuinely open — the in-winding NV sensor's neutron tolerance — is quantified in §9 and does not enter any structural margin.

§ 7

Benchmarking against published experiment and theory

The Kronos design targets are meaningful only against the demonstrated state of the art, and figure 22 and table 6 place them there.

FIELD

The field envelope of figure 5 is consistent with the demonstrated record: a REBCO solenoid has reached $45.5\,T$ [5], a reactor-scale toroidal-field model coil has reached $20.1\,T$ on the conductor [13,19,10], and an all-GdBCO no-insulation user magnet has reached $26.4\,T$ [6]. The Kronos centrepost, at $16.84\,T$, sits below the demonstrated model-coil field; the plug design field of $26.49\,T$ sits essentially at the no-insulation-user demonstration and between the model-coil and solenoid records — so neither magnet asks the conductor for a field beyond what the literature has shown, and the $35\,T$ conductor-capability point remains a claim about the tape rather than a coil record.

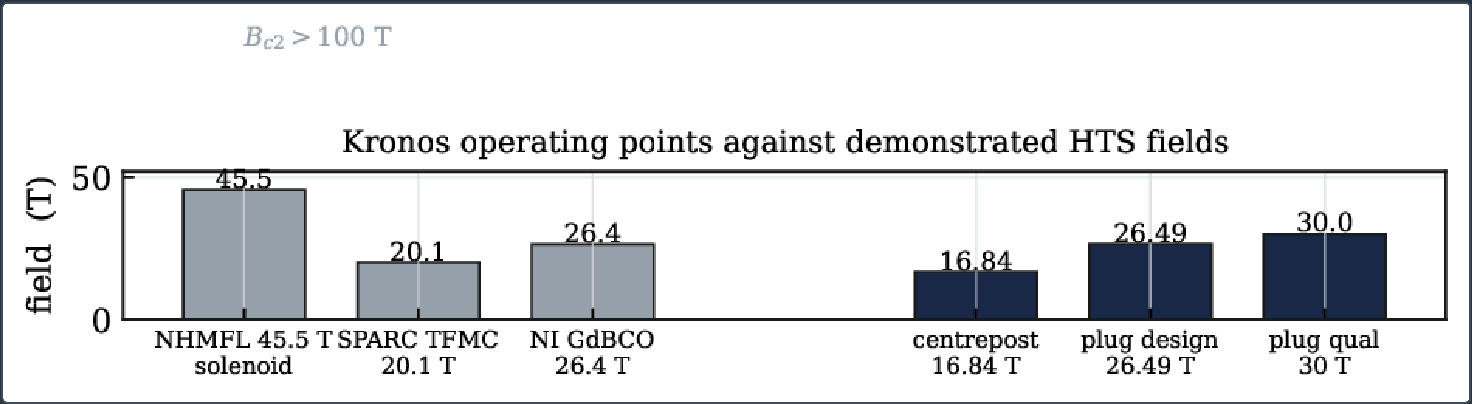

Kronos operating points against demonstrated HTS fields: the NHMFL $45.5\,T$ solenoid [5], the SPARC $20.1\,T$ toroidal-field model coil on conductor [13], and the $26.4\,T$ no-insulation GdBCO user magnet [6], beside the centrepost, plug design and plug qualification fields. All sit far below $B_{c2} > 100\,T$.

THE LOW-TEMPERATURE-SUPERCONDUCTOR CONTRAST

The magnitude of the REBCO advantage is clearest against the mature low-temperature-superconductor (LTS) alternative. The ITER magnet system, the largest superconducting-magnet project built, uses Nb_3Sn cable-in-conduit conductor and delivers a peak field on conductor of $\sim 12\,T$ at very large scale [14]; the field ceiling is set by the conductor's upper critical field ($B_{c2} \approx 25\,T$ for Nb_3Sn, with the practical operating field a fraction of that) and by the strain sensitivity of the brittle A15 phase. REBCO's $B_{c2} > 100\,T$ (figure 5) lifts that ceiling by roughly a factor of four, and it is that headroom — not any advantage in engineering current density at low field — that lets the Kronos centrepost run at $16.84\,T$ and the plug at $26.49\,T$ while remaining, respectively, at only 0.17 and 0.26 of the material limit. The price of the REBCO pathway is the winding mechanics this paper is about: where the LTS designer is limited by the conductor, the REBCO designer is limited by the structure, which is a more favourable place to be because structure responds to engineering (reinforcement, preload, bore) whereas a conductor's B_{c2} does not.

STRESS AND STRAIN

The SPARC model coil accommodated close to $1\,GPa$ of structural stress and $\sim 815\,kNm$ of Lorentz loading in a no-insulation architecture [13]; the Kronos plug's $\sim 814\,MPa$ thin-wall conductor hoop stress, closing to a $1.34\times$ margin on the real CAD, is squarely inside that demonstrated envelope. The 0.40% irreversible-strain ceiling of equation (19) is taken directly from van der Laan's and Osamura's systematic measurements of the reversible and irreversible strain limits of coated conductors [1,2], and the temperature-dependent winding moduli from the cryogenic electro-mechanical database [3]. The bore-resolved agreement of finite-element and closed-form Lam\'e (figures 7, 8) places the reinforcement budget on the standard elasticity of pressurised thick cylinders [36,37], and the sub-metre reinforcement of figure 9 is within the overwrap and structural practice assumed in conceptual HTS fusion-magnet designs [18,12,11].

IRRADIATION

The finding that a lifetime-limited winding prefers un-doped tape (figure 14) is consistent with the systematic fast-neutron studies that report coated-conductor I_c degrading in a manner sensitive to the pinning microstructure, with artificial-pinning-centre tapes degrading at lower fluence [16,15], and with the in-situ radiation-damage measurements on coated conductors held below T_c [17]. The NRT/arc-dpa rulers [27,28] set the dpa-to-fluence conversion, and the fusion-magnet radiation constraints are those surveyed for HTS fusion magnets [12].

QUENCH AND SENSING

The fused detector (figures 18, 17) should be read against the slow-normal-zone-propagation problem that Marchevsky makes quantitatively [30]: in HTS conductors a hot spot can reach damaging temperature before a resistive voltage appears, so voltage detection alone is inadequate. Our result is complementary to, and evaluated in a harder regime than, the fibre-optic thermometry Salazar demonstrated on VIPER cable at SULTAN [31] and the current-distribution monitoring Teyber showed for fusion cables [32]: the ROC is computed with per-sample signal-to-noise set well below the design-basis fault, and it is precisely in that weak-fault corner that channel fusion recovers early, low-false-alarm warning. The picotesla in-winding NV sensitivity sits comfortably inside the ensemble-NV envelope of the quantum-sensing literature [33,34,35].

@L L L>X@ QUANTITY	KRONOS TARGET	DEMONSTRATED / MEASURED	SOURCE
peak field, plug	$26.49\,T$	$26.4\,T$ (NI GdBCO); $45.5\,T$ (insert)	[6,5]
peak field, centrepost	$16.84\,T$	$20.1\,T$ on conductor (TFMC)	[13]
conductor hoop stress	$\sim 814\,MPa$ (thin wall)	$\sim 1\,GPa$ accommodated (TFMC)	[13]
irreversible strain	0.40% ceiling	measured 0.3–0.5%	[1,2]
APC vs un-doped life	un-doped $1.48\times$	APC degrades earlier	[16,15]
NV magnetometry	$0.189\,picoT\,\mathrm{Hz}^{-1/2}$	ensemble-NV envelope	[34,33]

Benchmarks. Kronos design targets against demonstrated HTS-magnet practice and the measured conductor limits they rely on.

§ 8

Design implications

Three implications follow from the analysis. First, because the conductor is nowhere near its field ceiling (§4.1) and the binding limits are winding strain (plug) and neutron life (centrepost), the productive levers are structural and nuclear, not superconducting: the graded pre-load of §2.6 and the inboard shield of §2.12 buy more than any conductor upgrade would. Second, the two magnets should be engineered, qualified and controlled separately, on their own critical surfaces (§4.6); a single "Kronos magnet" abstraction would mis-price both. Third, the material choices invert the usual room-temperature optimisation: the fusion neutron environment selects the un-doped tape over the higher-I_c doped tape (§4.8), and selects a graphene-aluminium bypass and a V_2O_3 self-protecting interlayer over a conventional copper stabiliser (§4.2). The magnet that results is conservative in field, aggressive in structural method, and honest about the one open sensor item.

A fourth implication is architectural. Because the same $B^2/2\mu_0$ scaling links stored energy, bore pressure and protection difficulty (§2.11), the productive protection choice is not a faster external dump but a self-protecting winding whose detection is fast enough that the MIITs budget is never approached; this is the reasoning behind the NI/MI-with-smart-interlayer choice of §5 and the fused precursor of §4.12. Taken together, the four implications point to a coherent programme: qualify each magnet on its own critical surface, buy margin with structure and shielding rather than with conductor field, select materials for the neutron environment rather than for room-temperature critical current, and protect by self-shedding plus early detection rather than by brute-force energy extraction. Each of these is developed in a dedicated companion paper — the plug structure in [49], the centrepost neutronics and life in [44,45], the conductor materials in [46,47], the quench sensing in [48], and the cold mass in [50] — and this paper is their shared superconductor-basis foundation.

§ 9

Limitations

Nothing here has been fabricated or measured: every number is a design target, a model output, or an inference from public REBCO literature. Four caveats bound the claims. First, the strain-first envelope of figure 11 is derived from the frozen finite-element anchors through the $p_{\mathrm{mag}} \propto B^2$ scaling with a field-independent thermal/vertical offset; the anchors are finite-element, but the field-swept envelope between them is a model, not a per-field measurement. Second, the critical-surface curves of figure 12 are an engineering parametrisation (equation 22); only the two operating-point margins are register anchors. Third, two conductor elements are reported as open in the register: the graphene-reinforced aluminium bypass is unsupported by data at the operating field, and a specific reinforcement-as-epitaxial-substrate route is infeasible; the structural case does not depend on either. Fourth, and most important, the quench-precursor metrics are twin-synthetic, and the in-winding NV sensor's neutron tolerance is the one open engineering item: its damage-to-lifetime margin factor is **39**, mitigated by shielded siting, a replaceable cartridge and a model-fusion backup, and it is to be closed by a dedicated irradiation study. A generic, self-proposed validation roadmap accompanies the analysis in the register [39].

§ 10

Conclusion

The REBCO high-field superconductor is the enabling basis of both Kronos machines, and its binding limit is winding strain, not conductor current. Setting the governing mechanics down as explicit, fully-derived equations — the Maxwell-stress reduction of the Lorentz body force, the winding-elasticity boundary-value problem, its closed-form Lam\'e reduction, the first-principles graded pre-load, the critical-surface margin, the no-insulation charging electrodynamics, the adiabatic quench integral, and the neutron-fluence life law — and reducing them to practice under one bore-resolved finite-element method benchmarked against the closed form and against a three-dimensional CAD-faithful analysis, we find that both magnets qualify. The breeder centrepost is stress-comfortable at $16.84\,T$ (load fraction 0.27, $\Delta T \approx 49.5\,K$), its binding limit the neutron life of a 0.58-full-power-year scheduled cartridge; the burner plug meets its $667\,MPa$ allowable at its required bore at $26.49\,T$ (load fraction 0.43, $\Delta T \approx 37.1\,K$), with a graded per-turn pre-load cutting the peak REBCO hoop strain by 52.4% to hold the winding under the 0.40% irreversible limit. The two magnets are modelled as the distinct devices they are, never conflating $16.84\,T$ with $26.49\,T$. The value of the work is the strain-first method — the per-turn pre-load and the per-coil, measured-margin qualification — and every number is a design target, not a Kronos measurement.

Acknowledgments tocsectionAcknowledgments Part of the Kronos Fusion Energy 2026 design series. The authors thank the Kronos physics de-risking programme for the frozen result set underlying every quantitative claim, and R J Weggel and C Weggel for the high-field-magnet design basis.

Reproducibility. Every headline quantity in this paper is a frozen anchor (BU-L1-A2, SC-BU-1, SC-BR-4, HX-09, HX-10, HX-11, BR-L1-A13b, BR-L2-A36, BR-CX-22, KX-L1-A15, KX-L1-A20, KX-L1-A22) in the Kronos Physics De-Risking Register [39] (doi:10.5281/zenodo.22133057) and is regenerable from the deposited figure-generation scripts and the open, CC-BY-4.0 series deposits. This paper is archived at doi:10.5281/zenodo.22645697; official version: https://www.kronosfusionenergy.com/publications/magnets.html. No result depends on unpublished or proprietary data, and no economic quantity enters the analysis.

Scope — what this paper does not claim. The $35\,T$ figure is a conductor field-capability claim, not a coil record; the high-field plug-coil feasibility is finite-element and CAD-FEA based, not a built and tested magnet.

Data availability tocsectionData availability The field, stress, strain, load-line, neutron-life, irradiation, cryogenic, conductor-quantity and precursor data used for the figures are archived with the deposit at doi:10.5281/zenodo.22645697 and trace to the register [39] by the serial identifiers cited inline. Any economic analysis is reported separately and is not part of the public deposit.

Competing interests tocsectionCompeting interests Provisional patent applications relating to aspects of this work — in particular the graded per-turn pre-load winding method — have been filed.

§ 11

Derivation of the magnetic pressure from the Maxwell stress tensor

For a magnetostatic field the force per unit volume is $\mathbf{f} = \mathbf{J} \times \mathbf{B} = (\nabla \times \mathbf{B}/\mu_0) \times \mathbf{B}$. Using the identity $(\nabla \times \mathbf{B}) \times \mathbf{B} = (\mathbf{B} \cdot \nabla)\mathbf{B} - \frac{1}{2}\nabla B^2$, the force is the divergence of the Maxwell stress tensor $\overleftrightarrow{T}_M = \mu_0^{-1}(\mathbf{BB} - \frac{1}{2}B^2\overleftrightarrow{I})$, so that $\mathbf{F} = \int_V \nabla \cdot \overleftrightarrow{T}_M \, \mathrm{d}V = \oint_S \overleftrightarrow{T}_M \cdot \mathrm{d}\mathbf{S}$. For a long solenoid with axial field $B\hat{\mathbf{z}}$ inside the bore and ≈ 0 outside, take the surface S to be a thin pillbox straddling the winding wall with normal $\hat{\mathbf{r}}$. The normal traction is $\hat{\mathbf{r}} \cdot \overleftrightarrow{T}_M \cdot \hat{\mathbf{r}} = \mu_0^{-1}(B_r^2 - \frac{1}{2}B^2)$. With $B_r \approx 0$ at the wall this is $-B^2/2\mu_0$ on the inside face and 0 on the outside, a net outward normal load of magnitude $p_{\mathrm{mag}} = B^2/2\mu_0$, which is equation (4). The tangential Maxwell stress integrates to zero around the closed winding, leaving the pure radial burst pressure that drives the hoop tension.

§ 12

Derivation of the Lam\'e reinforcement budget

For a uniform-property reinforced cylinder ($f_r = 0$ in the wall, internal pressure p_{mag} on the bore $r = a$, traction-free outer $r = b$), the homogeneous Navier equation (10) has the general solution $u(r) = C_1 r + C_2/r$. Imposing $\sigma_r(a) = -p_{\mathrm{mag}}$ and $\sigma_r(b) = 0$ through the constitutive law (9) fixes the constants and yields the Lam\'e stresses

$$\sigma_r(r) = \frac{a^2 p_{\mathrm{mag}}}{b^2 - a^2}\left(1 - \frac{b^2}{r^2}\right), \qquad \sigma_\theta(r) = \frac{a^2 p_{\mathrm{mag}}}{b^2 - a^2}\left(1 + \frac{b^2}{r^2}\right),$$

the second of which is equation (13). The hoop stress is maximal at $r = a$, giving equation (14); setting $\sigma_\theta(a) = \sigma_{\mathrm{allow}}$ and inverting for b gives the required wall of equation (15). The budget is finite only for $p_{\mathrm{mag}} < \sigma_{\mathrm{allow}}$, satisfied at all three plug fields (figure 9).

§ 13

Derivation of the graded pre-load that flattens the strain

Let the energised Lorentz hoop strain be $\varepsilon_L(r) = \sigma_\theta(r)/E_\theta$ with $\sigma_\theta(r)$ from (29). Writing $\beta_g \equiv a^2 p_{\text{mag}}/[(b^2 - a^2)E_\theta]$, $\varepsilon_L(r) = \beta_g(1 + b^2/r^2)$, which is maximal at the bore, $\varepsilon_L(a) = \beta_g(1 + b^2/a^2)$, and minimal at the outer turn, $\varepsilon_L(b) = 2\beta_g$. Imposing a per-turn compressive pre-strain $\varepsilon_{\text{pre}}(r)$ during winding, the net operating strain is $\varepsilon_{\text{net}}(r) = \varepsilon_L(r) - \varepsilon_{\text{pre}}(r)$. Demanding $\varepsilon_{\text{net}}(r) = \varepsilon_\star$ constant gives $\varepsilon_{\text{pre}}(r) = \varepsilon_L(r) - \varepsilon_\star = \beta_g(1 + b^2/r^2) - \varepsilon_\star$, which is equation (17). For the pre-strain to be physically realisable (compressive, $\varepsilon_{\text{pre}} \geq 0$) at every turn including the outermost, one needs $\varepsilon_\star \leq \varepsilon_L(b) = 2\beta_g$; choosing the limiting $\varepsilon_\star = 2\beta_g$ gives the peak-reduction ratio

$$\frac{\varepsilon_{\text{net}}^{\max}}{\varepsilon_L^{\max}} = \frac{2\beta_g}{\beta_g(1 + b^2/a^2)} = \frac{2a^2}{a^2 + b^2} = \frac{2}{1 + (b/a)^2},$$

equation (18). For a winding whose reinforced outer radius is a modest multiple of its bore, $(b/a)^2$ is of order two to three, so the ratio (30) lies well below unity, consistent with the register's 52.4% reduction ($0.595\% \to 0.283\%$). The gradient (spread between bore and outer strain) collapses from $\varepsilon_L(a) - \varepsilon_L(b) = \beta_g(b^2/a^2 - 1)$ to zero in the idealisation, i.e. the roughly fourfold flattening the finite-element model realises once finite winding tension is accounted for.

§ 14

Finite-element discretisation of the Navier–Lam\'e problem

The weak form of (10) multiplies the equilibrium equation by a test displacement $w(r)$ and integrates over the annulus with the cylindrical weight r:

$$\int_a^b \Big[\sigma_r \,\frac{\mathrm{d}w}{\mathrm{d}r} + \sigma_\theta \,\frac{w}{r}\Big] r\,\mathrm{d}r = \int_a^b f_r\, w\, r\,\mathrm{d}r,$$

the boundary terms vanishing under the traction-free conditions. Interpolating $u(r) = \sum_j N_j(r) u_j$ with quadratic shape functions N_j and using the same basis for w (Galerkin) turns (31) into the linear system $\mathbf{K}\mathbf{u} = \mathbf{f}$, with the element stiffness

$$K_{ij}^{(e)} = \int_{r_e}^{r_{e+1}} \Big[C_{rr} N_i' N_j' + C_{r\theta}\big(N_i' \tfrac{N_j}{r} + \tfrac{N_i}{r} N_j'\big) + C_{\theta\theta}\tfrac{N_i N_j}{r^2}\Big] r\,\mathrm{d}r,$$

where $C_{rr}, C_{r\theta}, C_{\theta\theta}$ are the plane-strain moduli of (9), assigned per element to carry the property grading (equations 11–12). Assembly, application of the pre-strain as an initial-strain load vector, and direct solution yield $u(r)$ and thence $\sigma_\theta(r)$; h-refinement to the 0.3%-convergence stated in §3.5 fixes the element count.

§ 15

The MIITs material integral

Under the adiabatic assumption (no heat leaves the hot zone on the protection timescale), the local energy balance is $\rho(T)J^2 = C(T)\,\mathrm{d}T/\mathrm{d}t$, where J is the current density in the stabiliser, $\rho(T)$ its resistivity and $C(T)$ the composite volumetric heat capacity. Separating variables and integrating from the operating temperature to the hot-spot limit T_{max},

$$\int_0^{t_{\mathrm{dump}}} J^2\,\mathrm{d}t = \int_{T_{\mathrm{op}}}^{T_{\mathrm{max}}} \frac{C(T)}{\rho(T)}\,\mathrm{d}T \equiv Z(T_{\mathrm{max}}),$$

which is equation (25); the left side is the current-density action (the “MIITs”, mega-amp-squared integrated over time, per unit area). For constant J this gives $t_{\mathrm{dump}} = Z(T_{\mathrm{max}})/J^2$. Because $C(T)$ rises steeply with temperature while $\rho(T)$ rises only weakly over the relevant range, $Z(T_{\mathrm{max}})$ grows faster than a constant, so the register anchors ($4\,s$ at 100 and $1.9\,s$ at $200\,A/mm^2$) lie slightly above the pure J^{-2} extrapolation plotted in figure 17.

§ 16

Mesh-convergence of the winding mechanics

The h-refinement study of §3.5 is summarised in table 7: as the number of radial quadratic elements spanning the winding annulus is increased, the peak bore hoop stress converges monotonically, the relative change between successive refinements falling below 0.3% once thirteen or more elements are used. The thirteen-node profiles of figures 7 and 8 are therefore taken from the converged branch, and the residual few-percent gap to the uniform-property closed form (§4.3) is physical — the resolution of the graded reinforcement — not a discretisation artefact.

RADIAL ELEMENTS	PEAK σ_θ (MPA)	CHANGE (%)
4	601.2	—
7	617.9	$+2.78$
10	623.1	$+0.84$
13	625.3	$+0.35$
20	626.9	$+0.26$
40	627.4	$+0.08$

Mesh convergence of the peak bore hoop stress for the graded-property winding (representative; finite-element integration of equations 7–10). The change between successive refinements falls below 0.3% at thirteen elements.

§ 17

Current-sharing temperature from the critical-surface parametrisation

Given the separable critical-surface fit of equation (22), the current-sharing temperature T_{cs} of equation (20) is obtained in closed form. At fixed field and angle, write $I_c(T) = I_c(B, T_{\text{op}})\left[(1 - T/T_c)/(1 - T_{\text{op}}/T_c)\right]^{\beta}$. Setting $I_c(T_{cs}) = I_{\text{op}}$ and denoting the operating load fraction $\lambda \equiv I_{\text{op}}/I_c(B, T_{\text{op}})$ gives

$$\left(\frac{1 - T_{cs}/T_c}{1 - T_{\text{op}}/T_c}\right)^{\beta} = \lambda \implies T_{cs} = T_c - \left(T_c - T_{\text{op}}\right)\lambda^{1/\beta},$$

so the margin is $\Delta T = T_{cs} - T_{\text{op}} = (T_c - T_{\text{op}})\left(1 - \lambda^{1/\beta}\right)$. The margin therefore grows as the load fraction λ falls and as the field-depressed T_c rises above the operating temperature; the centrepost, running at the lower field (higher T_c) and the lower load fraction ($\lambda = 0.27$), has the larger margin ($49.5\,K$), and the plug (T_c depressed by $26.49\,T$, $\lambda = 0.43$) the smaller ($37.1\,K$), exactly the ordering of figures 12 and 12. Equation (34) is the analytic backbone of those two figures; only the two operating-point margins are register anchors, the curves between being the parametrisation.

§ 18

Orthotropic homogenisation bounds of the winding pack

The Voigt (iso-strain) and Reuss (iso-stress) averages of equations (11)–(12) are the rigorous upper and lower bounds on the effective modulus of a two-phase (here multi-phase) composite: for any microstructure the true effective modulus lies between them, $E_{\text{Reuss}} \leq E_{\text{eff}} \leq E_{\text{Voigt}}$. For a layered winding pack the bounds are attained directionally — the hoop (in-tape) direction loads the layers in parallel and reaches the Voigt bound, while the radial direction stacks them in series and reaches the Reuss bound — so the winding is not merely bounded but genuinely orthotropic with $E_\theta = E_{\text{Voigt}}$ and $E_r = E_{\text{Reuss}}$. Tighter Hashin–Shtrikman bounds exist for statistically isotropic mixtures, but the layered geometry here makes the elementary Voigt/Reuss bounds exact for the two loading directions, which is why the plane-strain constitutive law of equation (9) is written with a single direction-appropriate modulus. For the constituent fractions and cryogenic moduli of §2.4 ($E_t \approx 180\,GPa$, $E_{Cu} \approx 120\,GPa$, $E_s \approx 200\,GPa$) the hoop modulus lands near $E_\theta \approx 150\,GPa$, and it is this value that maps the peak hoop stress of equation (14) to the peak strain of equation (19); the sensitivity of the governing strain to a $\pm 10\%$ excursion in E_θ is quantified in figure 20.

§ 19

Parameter set

Breeder centrepost: peak field $16.84\,T$, $B_0 = 8\,T$ on axis; $I_p = 9.66\,MA$; $R_0 = 1.20\,m$, $A = 2.5$, $\kappa = 2.0$, $\delta = -0.30$; neutron damage 18.85 dpa fpy^{-1}; cartridge life 0.58 fpy at $45\,cm$ WC; load fraction 0.27; $\Delta T \approx 49.5\,K$; CAD peak hoop strain 0.151% ($2.65\times$ margin); cold-mass load $\approx 5\,MW$ (HTS) vs $\approx 282\,MW$ (resistive). **Burner plug:** design field $26.49\,T$ (evaluation fields $17/26.49/30\,T$), $Q_E = 1.318$, $\eta_{\rm DEC} = 0.49$, $f_n = 5.44\%$; magnetic pressure $115/279/358\,MPa$; required reinforcement $0.16/0.48/0.71\,m$; reinforced allowable $667\,MPa$; FE peak $440\,MPa$ (utilisation 0.66); conductor hoop stress $\sim 814\,MPa$ thin-wall (margin 0.86) closing to $1.34\times$ on CAD; peak hoop strain 0.283% (graded pre-load), 0.365% (with thermal/vertical); load fraction 0.43; $\Delta T \approx 37.1\,K$; ampere-turn density $13.5\,MA/m$, $\approx 6.8 \times 10^4$ turns/m at $200\,A$, $\approx 4 \times 10^2$ km tape/m at $1\,m$ radius. **Conductor:** irreversible strain limit 0.40%; break-even fast fluence, un-doped 5.64×10^{22} vs pinned 3.82×10^{22} $/m^2$; graphene-Al stabiliser $\sim 2 \times 10^4$ $siemens/cm$ at cryo in 30–$35\,T$; NV sensitivity $0.189\,picoT$ Hz$^{-1/2}$, bandwidth 125 Hertz, $neutronmarginfactor$39; $MIITs$4 s/1.9 sat100/200 A/mm²\$.

APPARATUS

Portfolio, People & Record

The intellectual-property estate, the people who built it, the limitations that gate it, and the sources it rests on.

1	4	40	27
GRANTED PATENT	2026 PROVISIONALS	TEAM MEMBERS	2022 PROVISIONALS

INTELLECTUAL PROPERTY

The patent portfolio

The estate spans a granted high-field magnet patent, pending utility and 2026 provisional filings that map to the two products, a digital-twin control provisional, a registered trademark application, and the original 2022 provisional family. Every patentable disclosure in the five-paper arXiv drop was protected **before** publication: the breeder and burner provisionals were filed 1–2 August, and a publication-gap omnibus filing the evening before the drop swept up the DEC, plasma-control, and REBCO-winding matter of the three otherwise-unprotected papers. Patent numbers and application serials are matters of public record; claim scope is summarised, not reproduced.

GRANTED & PENDING UTILITY

US 12,009,112	High-field tilted graded-REBCO magnet architecture (KRONO-002A) · *app. 17/878,550*	GRANTED
US 17/878,507	Core device / method (KRONO-001A) · *utility*	PENDING

2026 PROVISIONAL FILINGS — MAPPED TO THE PRODUCTS

64/124,209	Hyperion — spherical-tokamak tritium / helium-3 foundry · *breeder · filed Aug 2026*	FILED
64/124,220	Aegis / MetroVolt — synchrotron-cutoff, fuel-selection & plug-winding · *generator · filed Aug 2026*	FILED
64/115,167	KRONOS-CTRL digital-twin plant control · *provisional · filed Jul 2026*	FILED
64/005,440	Integrated spherical-tokamak fusion architecture · *early integrated-architecture filing · filed Mar 2026*	FILED
64/105,530	Negative-triangularity spherical-tokamak architecture · *foundational ST filing · filed Jul 2026*	FILED
64/128,097	Publication-gap omnibus — quasineutral two-species expander DEC · provenance-gated / latency-split plasma control · as-built high-field winding & conductor architecture · *filed 7 Aug 2026, the evening before the arXiv drop*	FILED

TRADEMARK & ORIGIN

FTK-98801894	Kronos Fusion Energy — trademark application	FILED
KR-2022-*	Original provisional family (KR-2022-00001 … 00027) · *27 filings, 2022*	PRIORITY

The narrow, defensible magnet novelty — the specific conductor and the digital-twin winding optimisation, not high-field REBCO as a category — is the commercial core that can earn ahead of any $Q > 1$ milestone, with markets in fusion magnet supply, MRI/NMR, accelerators, and proton therapy. The claim is scoped honestly: the high field is a *system field* result, not a stand-alone-coil record; the small-bore plug coil is structurally infeasible as a bare winding but resolved by a stress-managed structural shield (feasible-pending-FEA); and the winding-tape experiment returned a *null result*. The value is the method, not a field record.

THE TEAM

Founding partners, board, advisors & auditors

Kronos is built by a bench of advanced-fuel-fusion, high-field-magnet, direct-conversion, and materials specialists, with a board and operations team drawn from defense, national laboratories, and industry. Dates are shown as ranges; where a tenure has ended or is term-ending, the range says so.

FOUNDING PARTNERS — SCIENCE

Dr. Gerald Kulcinski
Co-Founder · Helium-3 & Advanced-Fuel Fusion
UW–Madison · 2023–Present

Dr. Carl Weggel
Chief Scientist / S.M.A.R.T. Design
MIT Alcator Program · 2022–Present

Dr. Robert J. Weggel
Magnetic Field Design
MIT Magnet Lab · 2022–Present

BOARD

Priyanca Ford
Founder & CEO · Executive Board
2022–Present

Bandel Carano
Finance / Strategy
Oak Investment Partners / Stanford · 2025–2026

Patrick Schweiger
Fusion Device Engineering
Oklo / CFS / TerraPower · 2025–Present

SCIENTIFIC ADVISORS

Dr. Steven O. Dean
Fusion Policy & History
DOE / Fusion Power Associates · 2025–Present

Dr. Patrick H. Diamond
Plasma Turbulence & Transport
UC San Diego · 2025–Present

Dr. Jack J. Dongarra
HPC & Numerical Algorithms
Turing Award · 2025–Present

Dr. Nasr M. Ghoniem
Chief Material Scientist
UCLA · 2025–Present

Dr. Siegfried Glenzer
Plasma Physics & Laser Fusion
Stanford / SLAC · 2022–Present

Dr. David A. Hammer
Pulsed-Power Fusion
Cornell · 2025–Present

Dr. Donald A. Spong
Plasma Theory & Confinement
ORNL · 2025–Present

Dr. Curtis Smith
Risk Assessment & Nuclear PRA
MIT / Idaho National Lab · 2025–Present

RADM (Ret.) David Goggins
Naval Engineering & Power-Plant Design
U.S. Navy · 2023–2026

Dr. Konstantin Batygin
Mathematician
Caltech · 2022–2025

Dr. Ruben Fair
Magnet Design / ITER Liaison
PPPL / Jefferson Lab · 2022–2025

Dr. Paul S. Weiss
Materials & Nanotechnology
UCLA · 2022–2025

SCIENTIFIC AUDITORS

Dr. Wilfred A. Cooper
Plasma Equilibrium Theory
EPFL / Swiss Plasma Center · 2025–Present

Dr. Ahmed Hassanein
Plasma–Material Interactions
Purdue / Argonne · 2025–Present

Dr. Patrick E. Hopkins
Extreme Thermal Materials
U. of Virginia · 2025–Present

Dr. Peter Hosemann
Materials Joining & Structural Integrity
UC Berkeley · 2025–Present

Dr. Travis W. Knight
Advanced Nuclear Fuels & Systems
U. of South Carolina · 2025–Present

Dr. Philippe Lebrun
Cryogenics & Magnet Cooling
CERN · 2025–Present

Dr. Nitendra Singh
Nuclear Safety & Fuel Cycle
ITER · 2025–Present

Dr. Guido Van Oost
Magnetic Confinement & Fusion Systems
Ghent University · 2025–Present

Dr. Gary S. Was
Radiation Materials & Structural Integrity
U. of Michigan · 2025–Present

Dr. Ray Sedwick
Direct Energy Conversion
U. of Maryland · 2025

OPERATIONS

Michael Laughlin
Chief Operating Officer
2022–Present

Martin Owens
Chief Strategy Officer
LANL / GE Hitachi · 2022–Present

MG (Ret.) Paul Pardew
Chief Contracting Officer
Army Contracting Command · 2022–Present

David Beck
Fusion Commercialization
U.S. Space Force · 2024–Present

Sushma Bhatia
Environmental & Legislative
Google · 2022–Present

Michael De Frenza
Technology Licensing
2023–Present

MG (Ret.) Robin L. Fontes
Cybersecurity & Defense
Army Cyber Command · 2022–Present

Vijay Gehani
Supply Chain & Components
INOX India · 2024–Present

Jon Michel Greenwood
IT & AI Infrastructure
Live Nation · 2023–Present

Brian C. O'Neill
National Security
CIA / ODNI · 2022–Present

Gen. (Ret.) Gustave F. Perna
DoD Liaison
Operation Warp Speed · 2022–2023

Andrea Romero
Marketing Lead
2022–Present

Legal counsel is retained; those roles are held on the internal roster and are not listed here.

SOURCES

References

1 D C van der Laan, J D Weiss and D M McRae, Status of CORC cables and wires for use in high-field magnets and power systems, and the irreversible strain limits of REBCO coated conductors, *Supercond. Sci. Technol.* **32** 033001 (2019). doi:10.1088/1361-6668/aafd66

2 K Osamura, M Sugano, S Machiya, H Adachi, S Ochiai and M Sato, Reversible strain limit of critical currents and universality of intrinsic strain effect for REBCO-coated conductors, *Supercond. Sci. Technol.* **22** 025015 (2009). doi:10.1088/0953-2048/22/2/025015

3 C Barth, G Mondonico and C Senatore, Electro-mechanical properties of REBCO coated conductors from various industrial manufacturers at 77 K, self-field and 4.2 K, 19 T, *Supercond. Sci. Technol.* **28** 045011 (2015). doi:10.1088/0953-2048/28/4/045011

4 D W Hazelton *et al*, Advances in high-field REBCO coated conductors for high-field magnet applications, *IEEE Trans. Appl. Supercond.* **30** 6600106 (2020). doi:10.1109/TASC.2020.2985934

5 S Hahn *et al*, 45.5-tesla direct-current magnetic field generated with a high-temperature superconducting magnet, *Nature* **570** 496 (2019). doi:10.1038/s41586-019-1293-1

6 S Yoon, J Kim, K Cheon, H Lee, S Hahn and S-H Moon, 26 T 35 mm all-$GdBa_2Cu_3O_{7-x}$ multi-width no-insulation superconducting magnet, *Supercond. Sci. Technol.* **29** 04LT04 (2016). doi:10.1088/0953-2048/29/4/04LT04

7 S Hahn, Y Kim, D K Park, K Kim, J P Voccio, J Bascu\ n\'an and Y Iwasa, No-insulation multi-width winding technique for high temperature superconducting magnet, *Appl. Phys. Lett.* **103** 173511 (2013). doi:10.1063/1.4826217

8 S Hahn, D K Park, J Bascu\ n\'an and Y Iwasa, HTS pancake coils without turn-to-turn insulation, *IEEE Trans. Appl. Supercond.* **21** 1592 (2011). doi:10.1109/TASC.2010.2093492

9 J L MacManus-Driscoll and S C Wimbush, Processing and application of high-temperature superconducting coated conductors, *Nat. Rev. Mater.* **6** 587 (2021). doi:10.1038/s41578-021-00290-3

10 A Molodyk *et al*, Development and large volume production of extremely high current density $YBa_2Cu_3O_7$ superconducting wires for fusion, *Sci. Rep.* **11** 2084 (2021). doi:10.1038/s41598-021-81559-z

11 D Uglietti, A review of commercial high temperature superconducting materials for large magnets: from wires and tapes to cables and conductors, *Supercond. Sci. Technol.* **32** 053001 (2019). doi:10.1088/1361-6668/ab06a2

12 P Bruzzone *et al*, High temperature superconductors for fusion magnets, *Nucl. Fusion* **58** 103001 (2018). doi:10.1088/1741-4326/aad835

13 Z S Hartwig *et al*, The SPARC toroidal field model coil program, *IEEE Trans. Appl. Supercond.* **34** 1 (2024). doi:10.1109/TASC.2024.3432613

14 N Mitchell and A Devred, The ITER magnets: design and construction status, *IEEE Trans. Appl. Supercond.* **22** 4200809 (2012). doi:10.1109/TASC.2011.2174560

15 R Prokopec, D X Fischer, H W Weber and M Eisterer, Suitability of coated conductors for fusion magnets in view of their radiation response, *Supercond. Sci. Technol.* **28** 014005 (2015). doi:10.1088/0953-2048/28/1/014005

16 D X Fischer, R Prokopec, J Emhofer and M Eisterer, The effect of fast neutron irradiation on the superconducting properties of REBCO coated conductors with and without artificial pinning centers, *Supercond. Sci. Technol.* **31** 044006 (2018). doi:10.1088/1361-6668/aaadf2

17 W Iliffe *et al*, In-situ measurements of the effect of radiation damage on the superconducting properties of coated conductors, *Supercond. Sci. Technol.* **34** 09LT01 (2021). doi:10.1088/1361-6668/ac1523

18 Y Zhai, D van der Laan, P Connolly and C Kessel, Conceptual design of HTS magnets for fusion nuclear science facility, *Fusion Eng. Des.* **168** 112611 (2021). doi:10.1016/j.fusengdes.2021.112611

19 A J Creely *et al*, Overview of the SPARC tokamak, *J. Plasma Phys.* **86** 865860502 (2020). doi:10.1017/S0022377820001257

20 D Whyte, Small, modular and economically attractive fusion enabled by high temperature superconductors, *Phil. Trans. R. Soc. A*

COLOPHON

How this document was made

The Kronos Fleet — Combined Editorial, 2026 is set in **Fraunces** (display), **Gelasio** (text), and **IBM Plex Mono** (data & equations), carried forward from the Kronos editorial design system.

The figures are rendered at 300 dpi from the deposited generator scripts; the document is composed as a single self-contained file with embedded fonts and imagery, paginated to US Letter, and rendered to PDF through a headless Chromium engine in matched light and dark editions.

Every headline quantity carries an evidence class; withdrawn and restated values are marked as such. Nothing herein is frozen beyond the founder-approved Tier-A set.

Explore it live — turn the interactive 3-D model, run the deposited solvers in the physics validator, and watch the companion film series.

LEGAL NOTICE

Notice, status, and distribution

Conceptual design & simulation study. This document reports a conceptual design and simulation study. It is not a construction commitment, a safety-analysis report, a regulatory filing, or an offer of securities. Forward-looking statements — schedules, costs, market sizes, and performance — are estimates subject to the limitations set out in the Simulations part and may change.

Numbers and their classes. Quantities are reported with evidence classes and case labels; modelled, assumed, and requirement-class values are identified as such and are not to be quoted without their labels.

Public edition. This edition carries the physics and design only; all financial, funding, and defense-commercial content has been removed for public distribution. The scientific text corresponds to the arXiv and journal submissions.

THE 2026 KRONOS SERIES

One programme, many papers

This editorial is one paper in the Kronos 2026 series — a real fusion company's complete, reproducible physics record for a spherical-tokamak breeder and its low-neutron D–^{3}He tandem-mirror burners. Every headline number is a frozen anchor in the Physics De-Risking Register.

Explore the whole programme: the De-Risking Register, the interactive 3-D model, and the physics validator.

KRONOS FUSION ENERGY

The REBCO High-Field Superconductor Basis: Conductor, Winding, and the Field Envelope for the Breeder Centrepost and Burner Plug

A real fusion company building real machines. Explore the science, live.

Zenodo · doi:10.5281/zenodo.22645697

Read on kronosfusionenergy.com

The Physics De-Risking Register